The Astrophysical Journal, 677:556–571, 2008 April 10

CS 22964−161: A DOUBLE-LINED CARBON- AND *s*-PROCESS–ENHANCED METAL-POOR BINARY STAR[1]

Ian B. Thompson,[2] Inese I. Ivans,[2,3] Sara Bisterzo,[4] Christopher Sneden,[2,5] Roberto Gallino,[4,6] Sylvie Vauclair,[7] Gregory S. Burley,[2] Stephen A. Shectman,[2] and George W. Preston[2]

Received 2007 October 15; accepted 2007 December 8

ABSTRACT

A detailed high-resolution spectroscopic analysis is presented for the carbon-rich low-metallicity Galactic halo object CS 22964−161. We have discovered that CS 22964−161 is a double-lined spectroscopic binary and have derived accurate orbital components for the system. From a model atmosphere analysis we show that both components are near the metal-poor main-sequence turnoff. Both stars are very enriched in carbon and in neutron-capture elements that can be created in the *s*-process, including lead. The primary star also possesses an abundance of lithium close to the value of the "Spite plateau." The simplest interpretation is that the binary members seen today were the recipients of these anomalous abundances from a third star that was losing mass as part of its AGB evolution. We compare the observed CS 22964−161 abundance set with nucleosynthesis predictions of AGB stars, discuss issues of envelope stability in the observed stars under mass transfer conditions, and consider the dynamical stability of the alleged original triple star. Finally, we consider the circumstances that permit survival of lithium, whatever its origin, in the spectrum of this extraordinary system.

Subject headings: binaries: spectroscopic — diffusion — nuclear reactions, nucleosynthesis, abundances — stars: abundances — stars: individual (CS 22964−161) — stars: Population II

1. INTRODUCTION

The chemical memory of the Galaxy's initial elemental production in short-lived early-generation stars survives in the present-day low-mass, low-metallicity halo stars showing starkly contrasting abundance distributions. Metal-poor stars have been found with order-of-magnitude differences in lithium contents, large ranges in α-element abundances (from $[\mathrm{Mg,\ Si,\ Ca,\ Ti/Fe}] < 0$ to $\sim$1),[8] nonsolar Fe peak ratios, and huge bulk variations in neutron-capture (*n*-capture) abundances.

One anomaly can be easily spotted in medium-resolution ($R \equiv \lambda/\Delta\lambda \simeq 2000$) spectroscopic surveys of metal-poor stars: large star-to-star variations in CH G-band strength, leading to similarly large carbon abundance ranges. Carbon-enhanced metal-poor stars (hereafter CEMP $\equiv [\mathrm{C/Fe}] \gtrsim +1$) are plentiful at metallicities $[\mathrm{Fe/H}] < -2$, with estimates of their numbers ranging from $\simeq$14% (Cohen et al. 2005) to $\gtrsim$21% (Lucatello et al. 2006). The large carbon overabundances are mainly (but not always) accompanied by large *n*-capture overabundances, which are usually detectable only at higher spectral resolution ($R \gtrsim 10{,}000$). In all but one of the CEMP stars discovered to date, the *n*-capture abundance pattern has its origin in slow *n*-capture synthesis (the *s*-process). The known exception is CS 22892−052 (e.g., Sneden et al. 2003b and references therein), which has $[\mathrm{C/Fe}] \sim +1$ but an *n*-capture overabundance distribution clearly consistent with a rapid *n*-capture (the *r*-process) origin. Properties of CEMP stars have been summarized recently in a large-sample high-resolution survey by Aoki et al. (2007). They conclude in part that the abundances of carbon and (*n*-capture) barium are positively correlated (their Fig. 6), pointing to a common nucleosynthetic origin of these elements in many CEMP stars.

CS 22964−161 was first noted in the "HK" objective prism survey of low-metallicity halo stars (Beers et al. 1992, hereafter BPS92). Using as a metallicity calibration the strength of the Ca II K line, BPS92 estimated $[\mathrm{Fe/H}] \simeq -2.62$. They also found CS 22964−161 to be one of a small group of stars with unusually strong CH G bands (see their Table 8). Recently, Rossi et al. (2005) analyzed a moderate-resolution spectrum of this star. From the extant *BVJK* photometry and distance estimate they suggested that CS 22964−161 is a subgiant: $T_{\mathrm{eff}} = 5750$ K and $\log g = 3.3$. Two metallicity estimates from the spectrum were in agreement at $[\mathrm{Fe/H}] = -2.5$, and three independent approaches to analysis of the overall CH absorption strength suggested a large carbon abundance, $[\mathrm{C/Fe}] = +1.1$.

We observed CS 22964−161 as part of a high-resolution survey of candidate low-metallicity stars selected from BPS92. When we discovered that the star shows very strong features of CH and *n*-capture species Sr II and Ba II, similar to many binary blue metal-poor (BMP) stars (Sneden et al. 2003a), we added it to a radial velocity monitoring program. Visual inspection of the next observation showed two sets of spectral lines, and so an intensive monitoring program was initiated on the du Pont and Magellan Clay telescopes at Las Campanas Observatory. In this paper we present our orbital and abundance analyses of CS 22964−161. Radial velocity data and the orbital solution are given in § 2, and broadband photometric information in § 3. We discuss the raw equivalent width measurements for the combined-light spectra and the extraction of individual values for the CS 22964−161 primary and secondary stars in § 4. Determination of stellar atmospheric parameters is presented in § 5, followed by abundance analyses of the individual stars in § 6 and of the CS 22964−161 system in § 7. Interpretation of the large lithium, carbon, and

[1] This paper includes data gathered with the 6.5 m Magellan and 2.5 m du Pont Telescopes located at Las Campanas Observatory, Chile.

[2] The Observatories of the Carnegie Institution of Washington, Pasadena, CA 91101; ian@ociw.edu, iii@ociw.edu, burley@ociw.edu, gwp@ociw.edu.

[3] Princeton University Observatory, Princeton, NJ 08544.

[4] Dipartimento di Fisica Generale, Università di Torino, 10125 Torino, Italy; bisterzo@ph.unito.it, gallino@ph.unito.it.

[5] Department of Astronomy and McDonald Observatory, University of Texas, Austin, TX 78712; chris@verdi.as.utexas.edu.

[6] Centre for Stellar and Planetary Astrophysics, Monash University, Clayton, VIC 3800, Australia.

[7] Laboratoire d'Astrophysique de Toulouse-Tarbes, Université de Toulouse, CNRS, Toulouse, France; sylvie.vauclair@ast.obs-mip.fr.

[8] We adopt the standard spectroscopic notation (Helfer et al. 1959) that for elements A and B, $\epsilon(\mathrm{A}) \equiv \log_{10}(N_{\mathrm{A}}/N_{\mathrm{H}}) + 12.0$ and $[\mathrm{A/B}] \equiv \log_{10}(N_{\mathrm{A}}/N_{\mathrm{B}})_{\star} - \log_{10}(N_{\mathrm{A}}/N_{\mathrm{B}})_{\odot}$. Also, metallicity is defined as the stellar [Fe/H] value.

TABLE 1
VELOCITY MEASUREMENTS FOR CS 22964−161

HJD (−2,440,000)	V_p (km s^{-1})	V_s (km s^{-1})	Phase
du Pont Observations			
13592.52532	24.79	41.04	0.0716
13592.56468	24.63	42.35	0.0718
13593.52234	25.34	38.32	0.0756
13593.56091	25.21	40.26	0.0757
13867.92873	36.59	27.00	0.1623
13870.91114	36.44	25.90	0.1741
13871.85817	37.22	26.27	0.1778
Magellan Observations			
13230.66465	38.43	25.01	0.6386
13580.79663	5.09	65.21	0.0252
13585.74591	14.80	52.79	0.0448
13587.62635	18.56	49.77	0.0522
13602.62780	32.29	...	0.1116
13603.50474	33.00	...	0.1151
13606.50536	33.83	...	0.1270
13631.67197	39.08	26.29	0.2266
13634.54878	39.06	25.43	0.2380
13817.90625	6.10	64.19	0.9642
13832.88449	4.11	66.51	0.0235
13834.88836	8.21	60.76	0.0314
13889.88563	40.09	25.83	0.2492
13890.73000	40.19	26.24	0.2526
13891.72338	40.03	25.80	0.2565
13891.79617	39.87	25.63	0.2568
13891.91199	39.79	25.33	0.2572
13892.72313	40.47	25.77	0.2604
13892.91348	40.03	25.21	0.2612
13893.76837	40.02	25.34	0.2646
13897.80466	40.22	24.87	0.2806
13898.72511	40.00	24.35	0.2842
13917.74748	40.82	23.51	0.3595
13919.72723	40.20	23.00	0.3674
13935.76042	41.08	23.66	0.4309
13938.71168	41.14	23.29	0.4426
13938.73591	41.10	23.53	0.4427
13951.57253	40.34	23.09	0.4935
13989.60930	38.73	25.04	0.6441
13990.59320	38.69	25.36	0.6480
14197.85590	40.80	23.87	0.4689
14258.82674	37.60	28.04	0.7088
14259.78553	37.50	27.81	0.7126
14316.78097	15.19	52.81	0.9383
14317.65762	13.63	53.75	0.9418
14328.67079	−4.33	74.49	0.9854
14329.70221	−5.60	75.71	0.9895
14333.56647	−5.03	75.31	0.0048
14334.49082	−3.13	74.78	0.0085
14335.48607	−1.45	72.22	0.0124
14336.53932	0.46	69.88	0.0166

s-process abundances in primary and secondary stars is discussed in § 8. Finally, we speculate on the nature of a former asymptotic giant branch (AGB) star that we suppose was responsible for creation of the unique abundance mix of the CS 22964−161 binary in § 9.

2. RADIAL VELOCITY OBSERVATIONS

We obtained observations of CS 22964−161 with the Clay 6.5 m MIKE (Bernstein et al. 2003) and du Pont 2.5 m echelle spectrographs. Properties of the two spectrographs are presented at the LCO Web site.[9] The Clay MIKE data have $R \equiv \lambda/\delta\lambda 40000$ and continuous spectral coverage for 3500 Å $\lesssim \lambda \lesssim$ 7200 Å. The du Pont data have $R \simeq 25{,}000$, and out of the large spectral coverage of those data we used the region 4300 Å $\lesssim \lambda \lesssim$ 4600 Å for velocity measurements. Exposure times ranged from 1245 to 3500 s on the Clay telescope and from 3000 to 4165 s on the du Pont telescope. The observations generally consist of two exposures flanked by observations of a thorium-argon hollow-cathode lamp.

TABLE 2
ORBITAL PARAMETERS FOR CS 22964−161

Parameter	Value
P (days)	252.481±0.043
T_0 (HJD −2,440,000)	13827.383±0.103
γ (km s^{-1})	32.85± 0.05
K_p (km s^{-1})	23.65±0.10
K_s (km s^{-1})	26.92±0.13
e	0.6564±0.0024
ω (deg)	188.54±0.39
σ_p (km s^{-1})	0.37
σ_s (km s^{-1})	0.56
Derived quantities:	
$A \sin i$ ($R_\odot$)	190.32±0.65
$M_p \sin^3 i$ ($M_\odot$)	0.773±0.009
$M_s \sin^3 i$ ($M_\odot$)	0.680±0.007

The Magellan observations were reduced with pipeline software written by Dan Kelson following the approach of Kelson (2003, 2008). Postextraction processing of the spectra was done within the IRAF ECHELLE package.[10] The du Pont observations were reduced completely with IRAF ECHELLE software.

Velocities were initially measured with the IRAF FXCOR package using MIKE observations of HD 193901 as a template, and a preliminary orbit was derived. The three MIKE observations of CS 22964−161 obtained at zero velocity crossing (phase $\simeq$ 0.11) were then averaged together to define a new template, hereafter called the syzygy spectrum. This spectrum has a total integration time of 10,215 s and signal-to-noise ratio S/N > 160 at 4260 Å. We remeasured the velocities using this new template with the TODCOR algorithm (Zucker & Mazeh 1994). The cross-correlations covered the wavelength interval 4130 Å $< \lambda <$ 4300 Å. The syzygy spectrum was also used extensively in our abundance analysis (§ 6).

The radial velocity data were fitted with a nonlinear least-square solution. We chose to fit to only the higher resolution and higher S/N Magellan data, using the du Pont data to confirm the orbital solution. The observations are presented in Table 1, which lists the Heliocentric Julian Date (HJD) of midexposure, the velocities of the primary and secondary components, and the orbital phases of the observations. The adopted orbital elements are listed in Table 2, and the adopted orbit is plotted in Figure 1. Of particular importance to later discussion in this paper are the derived masses: $M_p \sin^3 i = 0.773 \pm 0.009\ M_\odot$ and $M_s \sin^3 i = 0.680 \pm 0.007\ M_\odot$; the orbital inclination cannot be derived from our data.

We discuss the velocity residuals to the orbital solution further in § 9. Hereafter, references to individual spectra will be by the

[9] Available at http://www.lco.cl.

[10] IRAF is distributed by the National Optical Astronomy Observatory, which is operated by the Association of Universities for Research in Astronomy, Inc., under cooperative agreement with the NSF.

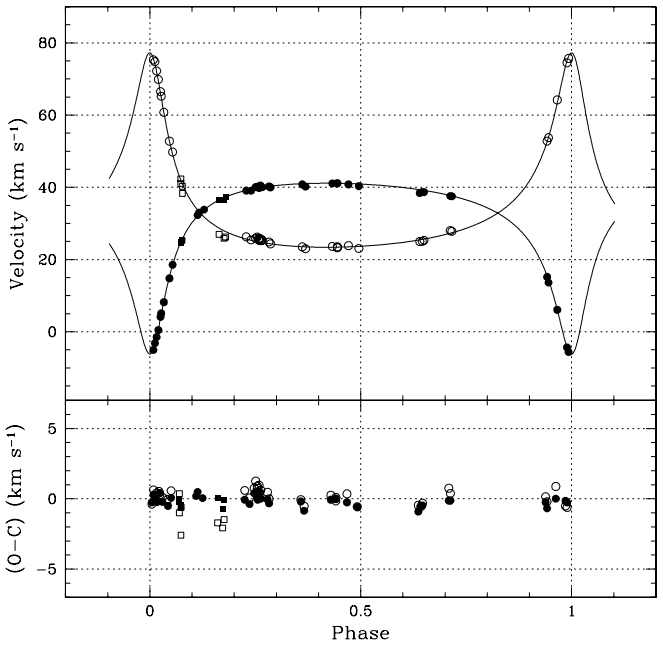

FIG. 1.—*Top*: Radial velocity observations of CS 22964−161 primary and secondary stars, and best-fit orbital solutions from these velocities. Circles represent data taken with MIKE on the Magellan Clay telescope, and squares represent data taken with the echelle spectrograph on the du Pont telescope. Filled symbols represent data for the primary, and open symbols are for the secondary. The lines are fits to the Magellan data only. *Bottom*: Differences of the observed velocities and the orbital solutions.

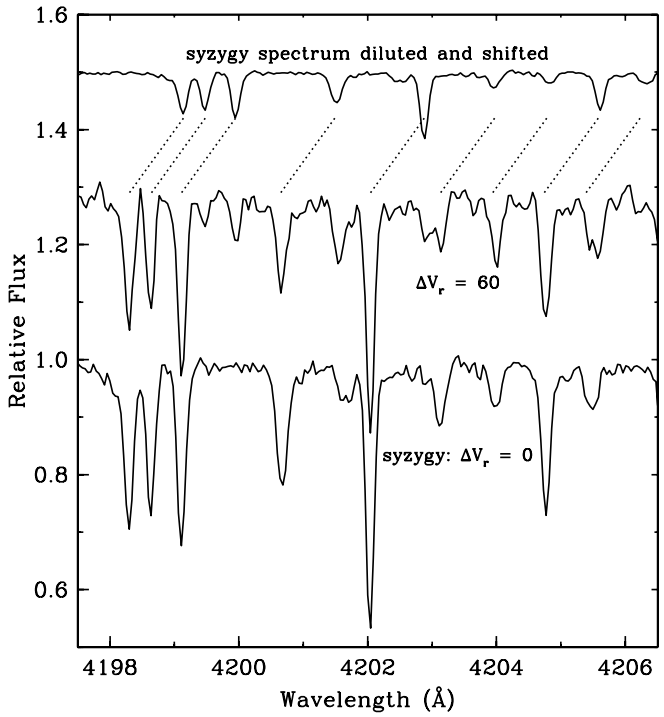

FIG. 2.—Observed composite absorption spectra of primary and secondary stars. The bottom spectrum is the spectrum at syzygy ($\Delta V_R = 0$ km s^{-1}); this is the mean of three individual observations. The middle spectrum is the mean of three observations obtained at phases with $\Delta V_R = 60$ km s^{-1}. The top spectrum represents the original syzygy spectrum after application of a velocity shift of 60 km s^{-1} and dilution by addition of a continuum flux that yields secondary line depths approximately matching those seen in the middle spectrum. Dotted lines point to secondary positions of a few lines that are very strong in the primary spectrum. The flux scale of the syzygy spectrum is correct, and the other two spectra have been vertically shifted in the figure for display purposes. The rest wavelength scale is that of the primary star.

HJD of Table 1, e.g., the spectrum obtained with Magellan MIKE on HJD 13817.90625 will be called "observation 13817."

3. PHOTOMETRIC OBSERVATIONS

Preston et al. (1991) list $V = 14.41$, $B - V = 0.488$, and $U - B = -0.171$ for CS 22964−161 based on a single photoelectric observation on the du Pont telescope. New CCD observations of this star were obtained with the du Pont telescope on UT 2006 May 28. The data were calibrated with observations of the Landolt standard field Markarian A (Landolt 1992). Observations of the standards and program object were taken at an air mass of ∼1.12, and we used standard extinction coefficients in the reductions. We derived $V = 14.43$ and $B - V = 0.498$ for CS 22964−161. Old and new photometric data are consistent with the typical ∼1% observational uncertainties in magnitudes, so we adopt final values of $V = 14.42$ and $B - V = 0.49$.

The ephemeris given in Table 2 predicts a primary eclipse at HJD 2,454,315.045 (2007 August 2, UT 13.08 hr) and a secondary eclipse at HJD 2,454,344.453 (2007 August 31, UT 22.87 hr). CS 22964−161 was monitored on the nights of 2007 August 2/3 and August 31/September 1 using the CCD camera on the Swope telescope at Las Campanas. Observations were obtained approximately every hour with a *V* filter. No variations in the *V* magnitude of CS 22964−161 in excess of 0.02 mag were detected.

4. EQUIVALENT WIDTH DETERMINATIONS

A double-line binary spectrum is a complex, time-variable mix of two sets of absorption lines and two usually unequal continuum flux levels. Following Preston (1994),[11] we define *observed* equivalent widths EW_o to be those measured in the combined-light spectra, and *true* equivalent widths EW_t to be those of each star in the absence of its companion's contribution. If the primary-secondary velocity separation is large, one can attempt to measure observed EWs of primary and secondary stars independently. If this can be accomplished, then true EWs can be computed from knowledge of the relative flux levels of the stars. In practice, the derivation of true EWs is complex and subject to large uncertainties.

In Figure 2 we illustrate the difficulties in deducing observed EWs for each star from the observed CS 22964−161 composite spectra. Recall that in the syzygy spectrum (the co-addition of three individual observations), there is no radial velocity separation, or $\Delta V_R \simeq 0$ km s^{-1}. The primary and secondary spectral lines coincide in wavelength, producing the simple spectrum shown at the bottom of Figure 2. In contrast, the middle spectrum in this figure was generated from spectra in which the velocity separation was large enough for primary and secondary lines to be resolved (hereafter called velocity-split spectra). We co-added three of these spectra that have similarly large velocity differences, $\Delta V_R \simeq 60$ km s^{-1} (observations 13580, 60.12 km s^{-1}; 13817, 58.09 km s^{-1}; and 13832, 62.40 km s^{-1}; Table 1). The weaker, redshifted secondary absorption lines are obvious from comparison of this and the syzygy spectrum.

Identification of the secondary absorption lines is clarified by inspection of the top spectrum in Figure 2. We created this artificial spectrum to mimic the appearance of the secondary by diluting the observed syzygy spectrum with the addition of a constant 3 times larger than the observed continuum and shifting that spectrum redward by 60 km s^{-1}. In this line-rich wavelength domain, the velocity shift yields a few cleanly separated primary and

[11] A similar kind of analysis of the very metal-poor binary CS 22876−032 has been discussed by Norris et al. (2000).

secondary absorption features. For example, Fe I λ4199.11 in the primary becomes λ4199.95 in the secondary, and observed EWs of both stars can be measured. More often, however, secondary lines are shifted to wavelengths very close to other primary lines, destroying the utility of both primary and secondary features. An example of this is the Fe I λ4198.33 line, which at $\Delta V_R \simeq 60$ km s^{-1} becomes λ4199.17 for the secondary star, which contaminates the Fe I λ4199.11 line of the primary star. The various blending issues, combined with the intrinsic weakness of the secondary spectrum, yield few spectral features with clean EW values for both primary and secondary stars.

4.1. *Equivalent Widths from Comparison of Syzygy and Velocity-Split Spectra*

In view of the blending issues outlined above, we derived the observed EWs through a spectrum difference technique. On the mean syzygy spectrum, we measured $\mathrm{EW}_{o,\mathrm{tot}} = \mathrm{EW}_{o,p} + \mathrm{EW}_{o,s}$, where subscript o denotes an observed EW and subscripts p and s denote primary and secondary stars, respectively. On five spectra with large primary-secondary velocity separations (13580, 13585, 13587, 13817, 13834) we measured the primary star lines, $\mathrm{EW}_{o,p}$. These five independent values were averaged, and then the secondary star's values were computed as $\mathrm{EW}_{o,s} = \mathrm{EW}_{o,\mathrm{tot}} - \langle \mathrm{EW}_{o,p} \rangle$. In this procedure we attempted to avoid primary lines that would have significant contamination by secondary lines in the velocity-split spectra.

The observed EW values are given in Table 3, along with the line excitation potentials and transition probabilities. In this table we also include the atomic data for lines from which abundances ultimately derived from synthetic spectrum rather than EW computations. For one estimate of the uncertainty in our EW measurement procedure, we computed standard deviations for the primary-star measurements of each line $\sigma\mathrm{EW}_{o,p}$. The mean and median of these values for the whole line data set were 5.2 and 4.1 mÅ, respectively. The uncertainties in $\mathrm{EW}_{o,\mathrm{tot}}$ are expected to be smaller because the syzygy spectrum is the mean of three individual observations and is thus of higher S/N. Therefore, we take 4–5 mÅ as an estimate of the uncertainty in $\mathrm{EW}_{o,s}$ values determined in the subtraction procedure.

For a few very strong transitions the secondary lines are deep enough to cleanly detect when they split away from the primary lines. We have employed these to assess the reliability of the EWs derived by the subtraction method described above. In Figure 3 we show a comparison of $\mathrm{EW}_{o,s}$ values given in Table 3 for seven lines that we measured on up to six velocity-split spectra (the five named in the previous paragraph plus 13832, which was not used in the subtraction procedure). Taking the means of the $\mathrm{EW}_{o,s}$ measurements of each line and comparing them to the subtraction-based values of Table 3, the average difference for the seven lines is 0.8 mÅ with a scatter $\sigma = 3.5$ mÅ (the median difference is 0.6 mÅ). This argues that in general the individual $\mathrm{EW}_{o,s}$ values agree with the $\mathrm{EW}_{o,s}$ subtraction-based ones.

Derivation of true EWs depends on knowledge of the relative luminosities of primary and secondary stars. Formally, from equations (4) and (5) of Preston (1994), we have $\mathrm{EW}_{p,t} = \mathrm{EW}_{p,o}(1 + l_s/l_p)$ and $\mathrm{EW}_{s,t} = \mathrm{EW}_{s,o}(1 + l_p/l_s)$, where subscript t represents the true EW and l stands for apparent luminosity. The luminosity ratios will be wavelength dependent if the two stars are not identical in temperature. For the entire line data set, ignoring weaker primary lines (those with $\mathrm{EW}_{p,o} < 25.0$ mÅ), we calculated a median equivalent width ratio $(\mathrm{EW}_{p,o}/\mathrm{EW}_{s,o}) = 5.2$. Inspection of the velocity-split spectra suggested that *relative* line strengths in the secondary spectrum were not radically different

TABLE 3
LINE LIST FOR CS 22964−161

Line	χ (eV)	log gf	$\mathrm{EW}_{p,o}$ (mÅ)	$\mathrm{EW}_{p,t}$ (mÅ)	$\mathrm{EW}_{s,o}$ (mÅ)	$\mathrm{EW}_{s,t}$ (mÅ)
Li I λ6707.80	0.00	+0.18	24	29	...	...
Mg I λ3829.36	2.71	−0.21	104	122	31	222
Mg I λ3832.31	2.71	+0.14	128	150	30	213
Mg I λ4703.00	4.35	−0.38	40	47	8	55
Mg I λ5172.70	2.71	−0.38	127	152	25	156
Mg I λ5183.62	2.72	−0.16	144	172	28	174
Mg I λ5528.42	4.35	−0.34	40	49	10	63
Al I λ3961.53	0.01	−0.34	62	73	11	79
Si I λ3905.53	1.91	+0.09	...	...	...	...
Ca I λ4226.74	0.00	+0.24	134	158	27	180
Ca I λ5349.47	2.71	−0.31	11	13	...	...
Ca I λ5588.76	2.53	+0.36	21	28	3	27
Ca I λ5857.46	2.93	+0.24	17	21	...	...
Ca I λ6102.73	1.88	−0.79	12	14	4	23
Ca I λ6122.23	1.89	−0.32	26	33	2	12
Ca I λ6162.18	1.90	−0.09	33	41	4	27
Ca I λ6439.08	2.52	+0.39	28	36	3	22
Sc II λ3645.31	0.02	−0.42	43	50	8	61
Sc II λ4246.84	0.31	+0.24	59	69	8	55
Ti II λ3477.19	0.12	−1.06	85	99	...	...
Ti II λ3510.85	1.89	+0.14	55	64	...	...
Ti II λ3596.05	0.61	−1.22	43	50	12	90
Ti II λ3641.34	1.24	−0.71	40	46	12	86
Ti II λ3759.30	0.61	+0.20	97	113	19	137
Ti II λ4394.06	1.22	−1.77	16	18	...	...
Ti II λ4443.80	1.08	−0.70	55	66	6	45
Ti II λ4444.56	1.12	−2.21	14	16	...	...
Ti II λ4468.49	1.13	−0.60	59	71	7	52
Ti II λ4501.27	1.12	−0.76	54	65	5	40
Ti II λ5336.79	1.58	−1.63	13	16	...	...
Cr I λ3578.69	0.00	+0.41	59	69	13	97
Cr I λ3593.50	0.00	+0.31	65	76	6	46
Cr I λ4254.33	0.00	−0.11	57	67	4	29
Cr I λ4274.80	0.00	−0.23	72	84	...	...
Cr I λ4289.72	0.00	−0.36	63	74	7	44
Cr I λ4646.17	1.03	−0.73	5	6	2	14
Cr I λ5206.04	0.94	+0.03	29	35	6	36
Cr I λ5409.79	1.03	−0.71	15	18	...	...
Cr II λ4558.65	4.07	−0.66	8	9	2	10
Cr II λ4588.20	4.07	−0.64	6	7	...	...
Mn I λ4030.76	0.00	−0.48	...	...	...	...
Mn I λ4033.06	0.00	−0.62	...	...	...	...
Mn I λ4034.49	0.00	−0.81	...	...	...	...
Fe I λ3475.46	0.09	−1.05	82	94	34	249
Fe I λ3476.71	0.12	−1.51	73	84	8	61
Fe I λ3490.59	0.05	−1.11	76	88	16	117
Fe I λ3497.84	0.11	−1.55	71	82	8	58
Fe I λ3521.27	0.91	−0.99	56	65	15	111
Fe I λ3554.94	2.83	+0.54	47	55	6	45
Fe I λ3558.53	0.99	−0.63	68	79	16	113
Fe I λ3565.40	0.96	−0.13	89	103	21	151
Fe I λ3570.13	0.91	+0.18	151	175	26	190
Fe I λ3581.21	0.86	+0.42	114	132	36	262
Fe I λ3606.69	2.69	+0.32	41	47	8	59
Fe I λ3608.87	1.01	−0.09	80	92	20	142
Fe I λ3618.78	0.99	+0.00	88	102	30	219
Fe I λ3631.48	0.96	+0.00	102	118	23	168
Fe I λ3647.85	0.91	−0.14	82	95	22	162
Fe I λ3679.92	0.00	−1.58	69	80	17	125
Fe I λ3687.47	0.86	−0.80	87	102	11	77
Fe I λ3727.63	0.96	−0.61	83	96	10	75
Fe I λ3745.57	0.09	−0.77	100	116	25	176
Fe I λ3745.91	0.12	−1.34	89	104	10	72
Fe I λ3758.24	0.96	−0.01	100	116	21	149

TABLE 3—*Continued*

Line	χ (eV)	log gf	EW$_{p,o}$ (mÅ)	EW$_{p,t}$ (mÅ)	EW$_{s,o}$ (mÅ)	EW$_{s,t}$ (mÅ)
Fe I λ3763.80	0.99	−0.22	86	99	15	106
Fe I λ3787.89	1.01	−0.84	69	80	10	71
Fe I λ3820.44	0.86	+0.16	114	133	22	157
Fe I λ3825.89	0.92	−0.02	99	116	22	153
Fe I λ3840.45	0.99	−0.50	74	87	20	140
Fe I λ3856.38	0.05	−1.28	84	98	11	76
Fe I λ3865.53	1.01	−0.95	67	79	11	76
Fe I λ3899.72	0.09	−1.51	70	81	19	135
Fe I λ3917.18	0.99	−2.15	27	31	4	27
Fe I λ3922.92	0.05	−1.63	75	87	16	110
Fe I λ3949.96	2.18	−1.25	18	21	6	38
Fe I λ4005.25	1.56	−0.58	61	71	12	85
Fe I λ4071.75	1.61	−0.01	79	92	17	125
Fe I λ4134.69	2.83	−0.65	19	22	4	29
Fe I λ4143.88	1.56	−0.51	68	80	8	53
Fe I λ4147.68	1.49	−2.07	12	14	4	29
Fe I λ4175.64	2.85	−0.83	18	21	...	...
Fe I λ4187.05	2.45	−0.51	38	45	2	16
Fe I λ4187.81	2.42	−0.51	42	49	6	41
Fe I λ4191.44	2.47	−0.67	26	30	8	54
Fe I λ4199.10	3.05	+0.16	52	61	...	...
Fe I λ4202.04	1.49	−0.69	62	72	13	85
Fe I λ4216.19	0.00	−3.36	24	28	2	13
Fe I λ4222.22	2.45	−0.91	24	28	...	...
Fe I λ4233.61	2.48	−0.58	37	43	4	24
Fe I λ4250.13	2.47	−0.38	47	56	...	...
Fe I λ4260.48	2.40	+0.08	61	72	10	69
Fe I λ4271.16	2.45	−0.34	58	69	20	131
Fe I λ4271.77	1.49	−0.17	93	109	11	77
Fe I λ4282.40	2.18	−0.78	34	39	8	52
Fe I λ4383.55	1.48	+0.21	104	122	15	100
Fe I λ4404.75	1.56	−0.15	76	90	14	92
Fe I λ4415.12	1.61	−0.62	62	73	16	108
Fe I λ4427.32	0.05	−2.92	37	44	10	65
Fe I λ4430.61	2.22	−1.73	10	12	2	15
Fe I λ4447.72	2.22	−1.34	19	22	4	27
Fe I λ4461.65	0.09	−3.19	20	24	8	52
Fe I λ4466.55	2.83	−0.60	19	22	9	59
Fe I λ4489.73	0.12	−3.90	6	6	3	20
Fe I λ4494.56	2.20	−1.14	23	27	3	20
Fe I λ4528.61	2.18	−0.89	35	42	8	51
Fe I λ4602.95	1.49	−2.21	13	15	2	16
Fe I λ4871.32	2.87	−0.36	25	29	5	34
Fe I λ4872.14	2.88	−0.57	25	30	...	...
Fe I λ4890.76	2.88	−0.39	24	29	10	65
Fe I λ4891.50	2.85	−0.11	37	44	8	49
Fe I λ4903.32	2.88	−0.93	12	14	...	...
Fe I λ4919.00	2.87	−0.34	29	34	6	35
Fe I λ5006.12	2.83	−0.61	23	28	...	...
Fe I λ5014.94	3.94	−0.27	12	15	4	22
Fe I λ5049.83	2.28	−1.35	18	21	8	49
Fe I λ5133.69	4.18	+0.20	11	13	7	45
Fe I λ5191.47	3.04	−0.55	21	25	...	...
Fe I λ5192.35	3.00	−0.42	30	36	...	...
Fe I λ5194.95	1.56	−2.02	17	25	...	...
Fe I λ5202.34	2.18	−1.84	11	13	...	...
Fe I λ5216.28	1.61	−2.08	16	19	...	...
Fe I λ5232.95	2.94	−0.06	39	48	3	29
Fe I λ5266.56	3.00	−0.39	24	29	4	21
Fe I λ5269.55	0.86	−1.33	70	86	15	98
Fe I λ5283.63	3.24	−0.52	17	20	3	20
Fe I λ5324.19	3.21	−0.10	25	30	...	...
Fe I λ5328.05	0.92	−1.47	68	81	13	82
Fe I λ5371.50	0.96	−1.64	55	66	12	77
Fe I λ5383.38	4.31	+0.65	17	20	...	...
Fe I λ5397.14	0.92	−1.98	47	56	5	32

TABLE 3—*Continued*

Line	χ (eV)	log gf	EW$_{p,o}$ (mÅ)	EW$_{p,t}$ (mÅ)	EW$_{s,o}$ (mÅ)	EW$_{s,t}$ (mÅ)
Fe I λ5405.78	0.99	−1.85	44	52	9	61
Fe I λ5429.71	0.96	−1.88	46	56	10	59
Fe I λ5434.53	1.01	−2.13	36	44	7	40
Fe I λ5446.92	0.99	−1.91	39	49	20	106
Fe I λ5501.48	0.96	−3.05	10	12	...	...
Fe I λ5506.79	0.99	−2.79	15	18	5	29
Fe I λ5569.63	3.42	−0.50	11	14	3	17
Fe I λ5572.85	3.40	−0.28	15	19	...	...
Fe I λ5586.77	3.37	−0.10	21	25	5	30
Fe I λ5615.66	3.33	+0.05	24	28	5	27
Fe I λ6136.62	2.45	−1.41	16	19	...	...
Fe I λ6191.57	2.43	−1.42	13	16	...	...
Fe I λ6230.74	2.56	−1.28	16	19	3	17
Fe I λ6393.61	2.43	−1.58	13	16	...	...
Fe I λ6400.01	3.60	−0.29	13	16	...	...
Fe I λ6430.85	2.18	−1.95	10	12	...	...
Fe I λ6494.98	2.40	−1.24	22	26	12	66
Fe II λ4178.86	2.57	−2.48	20	23	...	...
Fe II λ4233.17	2.58	−2.00	37	44	3	19
Fe II λ4508.28	2.84	−2.22	16	19	...	...
Fe II λ4555.89	2.82	−2.28	12	14	5	33
Fe II λ4923.92	2.89	−1.32	48	56	8	47
Fe II λ5234.62	3.22	−2.05	17	20	...	...
Fe II λ5275.99	3.20	−1.94	15	18	...	...
Co I λ3502.29	0.43	+0.07	52	61	11	81
Co I λ3506.33	0.51	−0.04	39	46	9	65
Ni I λ3472.56	0.11	−0.82	55	64	11	79
Ni I λ3483.78	0.27	−1.12	50	57	...	...
Ni I λ3500.86	0.17	−1.37	54	62	12	89
Ni I λ3510.33	0.21	−0.65	73	84	12	90
Ni I λ3515.07	0.11	−0.26	70	81	17	124
Ni I λ3519.76	0.27	−1.42	36	41	5	37
Ni I λ3524.54	0.03	−0.03	84	97	16	118
Ni I λ3566.39	0.42	−0.27	64	74	12	84
Ni I λ3597.71	0.21	−1.09	44	51	12	87
Ni I λ3619.40	0.42	−0.04	82	95	7	50
Sr II λ4077.71[a]	0.00	+0.17	(86)	(101)	(16)	(110)
Sr II λ4215.52[a]	0.00	−0.17	(80)	(94)	(15)	(99)
Y II λ3611.04	0.13	+0.01	...	...	...	...
Y II λ3710.29	0.18	+0.46	...	...	...	...
Y II λ3774.33	0.13	+0.21	...	...	...	...
Zr II λ4208.99	0.71	−0.46	...	...	...	...
Ba II λ4554.03[a]	0.00	+0.17	(92)	(108)	(13)	(82)
Ba II λ4934.10[a]	0.00	−0.16	(82)	(98)	(10)	(62)
Ba II λ5853.69	0.60	−0.91	...	...	...	...
Ba II λ6141.73[a]	0.70	−0.08	(58)	(71)	(8)	(46)
Ba II λ6496.91[a]	0.60	−0.38	(53)	(65)	(7)	(36)
La II λ3988.51	0.17	+0.21	...	...	...	...
La II λ3995.74	0.17	−0.06	...	...	...	...
La II λ4086.71	0.00	−0.07	...	...	...	...
La II λ4123.22	0.32	+0.13	...	...	...	...
Ce II λ4137.65	0.52	+0.44	...	...	...	...
Nd II λ4021.33	0.32	−0.10	...	...	...	...
Nd II λ4061.08	0.47	+0.55	...	...	...	...
Nd II λ4462.98	0.56	+0.04	...	...	...	...
Eu II λ3819.67	0.00	+0.51	...	...	...	...
Eu II λ3907.11	0.21	+0.17	...	...	...	...
Eu II λ3971.97	0.21	+0.27	...	...	...	...
Eu II λ4129.72	0.00	+0.22	...	...	...	...
Eu II λ4205.05	0.00	+0.21	...	...	...	...
Yb II λ3694.17	0.00	−0.30	...	...	...	...
Pb I λ4057.81	1.32	−0.17	...	...	...	...

[a] EW values are given for illustration only and were not used in final abundance determinations.

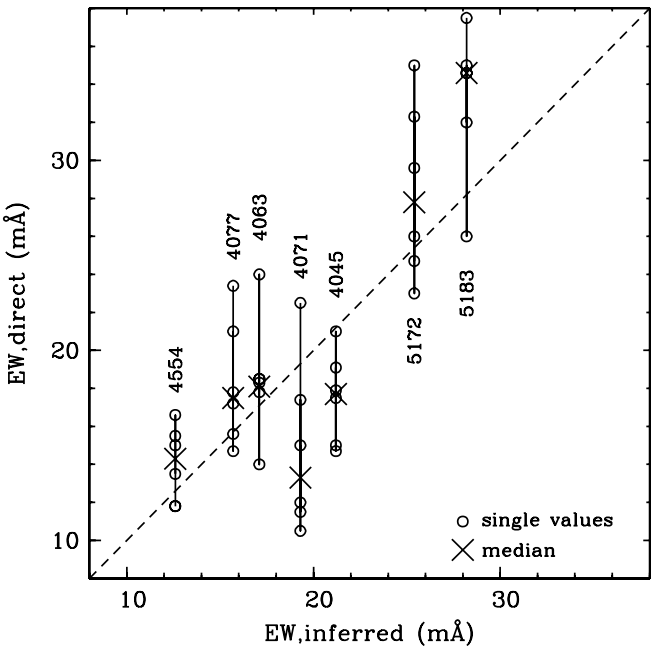

FIG. 3.—Comparison of observed equivalent widths of the secondary star inferred from the syzygy spectrum and those measured directly from the six spectra with large velocity splits between primary and secondary stars. Measurements for each spectral feature are connected by vertical lines and labeled with the feature wavelength. Medians of the EWs are displayed as crosses. The dashed slanting line indicates equality of EW values.

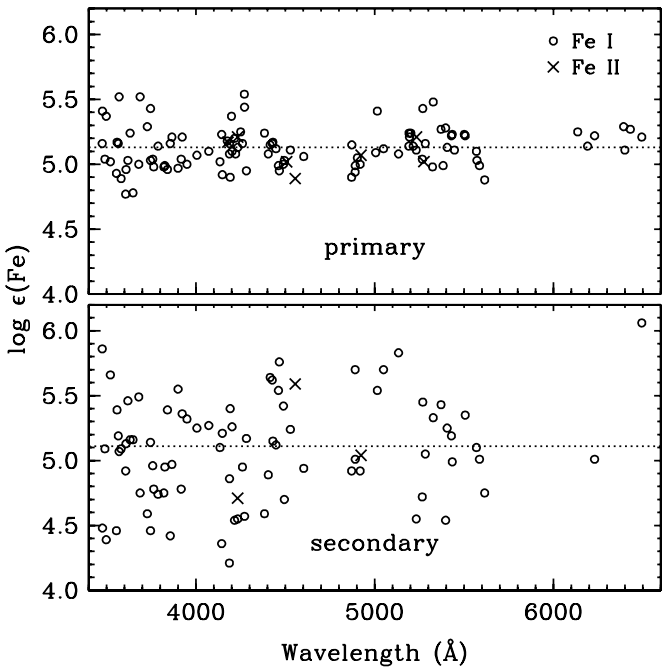

FIG. 4.—Iron abundances plotted as a function of wavelength for primary (*top*) and secondary (*bottom*) stars. The symbols are defined in the figure legend. Dashed horizontal lines are drawn to indicate the mean Fe I abundances of primary and secondary stars, $\epsilon(\mathrm{Fe}) = 5.13$ and 5.11, respectively.

from those of the primary spectrum. Therefore, we concluded that the spectral types of the stars are not too dissimilar and that to first approximation $\mathrm{EW}_{p,t} \sim \mathrm{EW}_{s,t}$. This assumption then leads to $\mathrm{EW}_{p,o}/\mathrm{EW}_{s,o} \sim l_p/l_s \sim 5$.

To account roughly for the small derived temperature difference (see § 5), we finally adopted $l_p/l_s = 5.0$ in the photometric V bandpass ($\lambda \simeq 5500$ Å) and increased the ratio linearly by a small amount with decreasing wavelength. Thus, in the B bandpass ($\lambda \simeq 4400$ Å) we used $l_p/l_s = 5.6$. Final true EW values using this prescription are given in Table 3. The correction factors between observed and true EWs were approximately 1.2 and 6.0 for primary and secondary stars in the V spectral region, and the disparity in these factors is larger at B. Clearly the $\mathrm{EW}_{p,t}$ values of Table 3 are much more reliably determined than the $\mathrm{EW}_{s,t}$ ones.

5. STELLAR ATMOSPHERE PARAMETERS

5.1. *Derivation of Parameters*

We used the observed $B - V$ color and minimum masses for the binary together with the Victoria-Regina stellar models (VandenBerg et al. 2006), to estimate initial model atmospheric parameters for the component stars of CS 22964−161. We adopted $B - V = 0.49$ from § 3 and $E(B - V) = 0.07$ (BPS92; a value we also estimate employing the dust maps of Schlegel et al. 1998) to obtain $(B - V)_0 = 0.42$. We assumed initially that $\sin^3 i \simeq 1.0$ for the binary orbit and thus $M_p = 0.773\ M_\odot$ and $M_s = 0.680\ M_\odot$, as derived in § 2. We interpolated the Victoria-Regina models computed for $[\mathrm{Fe/H}] = -2.31$, $[\alpha/\mathrm{Fe}] = +0.3$, and $Y = 0.24$, to obtain evolutionary tracks for these masses. These tracks were used to derive $B - V$ colors and luminosity ratios for the component stars. We adopted starting values of $T_{\rm eff}$, $\log g$, and l_p/l_s where the tracks give $B - V = 0.42$ for the combined system. These values were $T_{{\rm eff},p} = 6050$ K, $T_{{\rm eff},s} = 5950$ K and $\log g_p = 3.6$, $\log g_s = 4.2$. The luminosity ratios using these parameters were $l_p/l_s(B) = 8.65$ and $l_p/l_s(V) = 8.39$, somewhat larger than implied by our spectra.

Final model atmospheric parameters were found iteratively from the EW data for the two stars. We employed the LTE line analysis code MOOG[12] (Sneden 1973) and interpolated model atmospheres from the Kurucz (1998)[13] grid computed with no convective overshoot (as recommended by Castelli et al. 1997; Peterson et al. 2001).

We began by using standard criteria to estimate the model parameters of the CS 22964−161 primary: (1) for $T_{\rm eff}$, no trend of derived Fe I individual line abundances with excitation potential; (2) for v_t, no trend of Fe I abundances with EW; (3) for $\log g$, equality of mean Fe I and Fe II abundances (for no other element could we reliably measure lines of the neutral and ionized species); and (4) for model metallicity [M/H], a value roughly compatible with the Fe and α abundances. These criteria could be assessed reliably for the primary star because it dominates the combined light of the two stars. In the top panel of Figure 4 we illustrate the line-to-line scatter and (lack of) trend with wavelength of the primary's Fe I and Fe II transitions. With iteration among the parameters we derived $(T_{{\rm eff},p},\ \log g_p,\ v_{t,p},\ [\mathrm{M/H}]_p) = (6050 \pm 100\ \mathrm{K},\ 3.7 \pm 0.2,\ 1.2 \pm 0.3\ \mathrm{km\ s^{-1}},\ -2.2 \pm 0.2)$.

To estimate model parameters for the secondary, we assumed that derived [Fe/H] metallicities and abundance ratios of the lighter elements ($Z \leq 30$) in the primary and secondary stars should be essentially identical if they were formed from the same interstellar cloud. Iteration among several sets of ($T_{{\rm eff},s}$, $\log g_s$) pairs was done until $[\mathrm{Fe/H}]_s \simeq [\mathrm{Fe/H}]_p$ and Fe ionization equilibrium for the secondary was achieved. Given the weakness of the secondary spectrum and the resulting large correction factors used to calculate $\mathrm{EW}_{s,t}$ from $\mathrm{EW}_{s,o}$ values, it is not surprising that the spectroscopic constraints on the secondary parameters were weak.

[12] Available at http://verdi.as.utexas.edu/moog.html.
[13] Available at http://kurucz.harvard.edu/.

TABLE 4
INDIVIDUAL ABUNDANCE RESULTS FOR PRIMARY AND SECONDARY STARS

Species	$\log \epsilon_\odot$	$\log \epsilon_p$	σ_p	No.$_p$	$\log \epsilon_s$	σ_s	No.$_s$	$[X/H]_p$	$[X/H]_s$	$[X/Fe]_p$	$[X/Fe]_s$	Method
CH	8.70	7.64	0.10	...	7.44	0.40	...	−1.06	−0.86	+1.35	+1.15	syn
Fe I	7.52	5.13	0.16	104	5.11	0.44	83	−2.39	−2.41	+0.02	0.00	EW
Fe II	7.52	5.09	0.12	7	5.11	0.44	3	−2.43	−2.41	−0.02	0.00	EW
Na I	6.33	...	...	...	3.9	0.3	2	...	−2.4	...	0.0	syn
Mg I	7.58	5.53	0.20	6	5.52	0.15	6	−2.05	−2.06	+0.36	+0.35	EW
Al I	6.57	3.26	...	1	3.28	...	1	−3.31	−3.29	−0.90	−0.88	EW
Ca I	6.36	4.38	0.13	8	4.03	0.29	6	−1.98	−2.33	+0.43	+0.08	EW
Ti II	4.99	3.19	0.26	9	3.14	0.75	4	−1.80	−1.85	+0.61	+0.56	EW
Cr I	5.64	3.36	0.30	8	2.81	0.53	6	−2.28	−2.83	+0.13	−0.42	EW
Cr II	5.64	3.45	0.10	2	3.64	...	1	−2.19	−2.00	+0.22	+0.41	EW
Ni I	6.25	3.92	0.24	10	3.86	0.62	9	−2.33	−2.39	+0.08	+0.02	EW
Sr II	2.90	1.05	0.09	2	0.93	0.29	2	−1.85	−1.97	+0.56	+0.44	syn
Ba II	2.13	1.17	0.08	1	1.09	0.28	1	−0.96	−1.04	+1.45	+1.37	syn

This is apparent from the adopted Fe abundances displayed in the bottom panel of Figure 4. The σ-values for individual line abundances were about 3 times larger for the secondary than the primary (Table 4), and the number of transitions was substantially smaller (e.g., we measured seven Fe II lines for the primary but only three for the secondary).

We adopted final model parameters of ($T_{\rm eff,s}$, $\log g_s$, $v_{t,s}$, $[{\rm M/H}]_s$) = (5850 K, 4.1, 0.9 km s^{-1}, −2.2). Model uncertainties for the secondary were not easy to estimate and, of course, were tied to our opening assumption that the two stars have identical overall metallicities and abundance ratios. Thus, with $[{\rm M/H}]_p \equiv [{\rm M/H}]_s$, the uncertainties in $T_{\rm eff}$, $\log g$, and v_t of the secondary are approximately double their values quoted above for the primary. Thus, caution is obviously warranted in interpretation of the model parameters of the CS 22964−161 secondary.

5.2. *Comparison to Evolutionary Tracks*

The well-determined $T_{\rm eff,p}$ and $\log g_p$ values can be used with the mass and luminosity ratios of the stars to provide an independent estimate of $T_{\rm eff,s}$ and $\log g_s$. Standard relations $L \propto R^2 T_{\rm eff}^4$ and $g \propto M/R^2$ lead to

$$\log(L_s/L_p) = \log(l_s/l_p) = \log(M_s/M_p) + 4\log(T_{{\rm eff},s}/T_{{\rm eff},p}) - \log(g_s/g_p).$$

Taking an approximate average luminosity ratio to be $l_p/l_s \simeq 5.3$, adopting $M_s/M_p = 1.15$ (Table 2) and assuming $T_{\rm eff,p} = 6050$ K and $\log g_p = 3.7$ from above, we get a predicted temperature-gravity relationship $\log g_s \simeq 4 \log T_{\rm eff,s} - 10.8$.

In Figure 5 we show the very metal-poor main-sequence turnoff region of the H-R diagram in ($\log T_{\rm eff}$, $\log g$) units. The Victoria-Regina evolutionary tracks (VandenBerg et al. 2006; $[{\rm Fe/H}] = -2.31$, $[\alpha/{\rm Fe}] = +0.3$, and $Y = 0.24$) discussed in § 5.1 are again employed. However, the unknown binary orbital inclination of CS 22964−161 cannot be ignored here. Therefore, we have plotted the tracks for three pairs of masses corresponding to assumed sin i values of 90°, 80°, and 75°. Also plotted is a straight line representing the CS 22964−161 secondary star temperature-gravity equation derived above.

The CS 22964−161 primary and secondary and ($T_{\rm eff}$, $\log g$) positions are indicated with filled circles in Figure 5. We also add data indicated with open triangles from CEMP high-resolution spectroscopic studies for stars of similar metallicity, taken here to be $[{\rm Fe/H}] = -2.4 \pm 0.4$. The studies include those of Aoki et al. (2002), Sneden et al. (2003a), and Cohen et al. (2006). If $T_{\rm eff,s} = 5850$ K from the spectroscopic analysis, then the temperature-gravity relationship from above predicts $\log g_s = 4.3$ (indicated by a filled square in the figure). Our spectroscopic value of $\log g_s = 4.1$ lies well within the uncertainties of both estimates.

Given the apparently anomalous position of the CS 22964−161 secondary in Figure 5, it is worth repeating its abundance analysis using atmospheric parameters forced to approximately conform with the evolutionary tracks. This is equivalent to attempting a model near the high-temperature, high-gravity end of its predicted

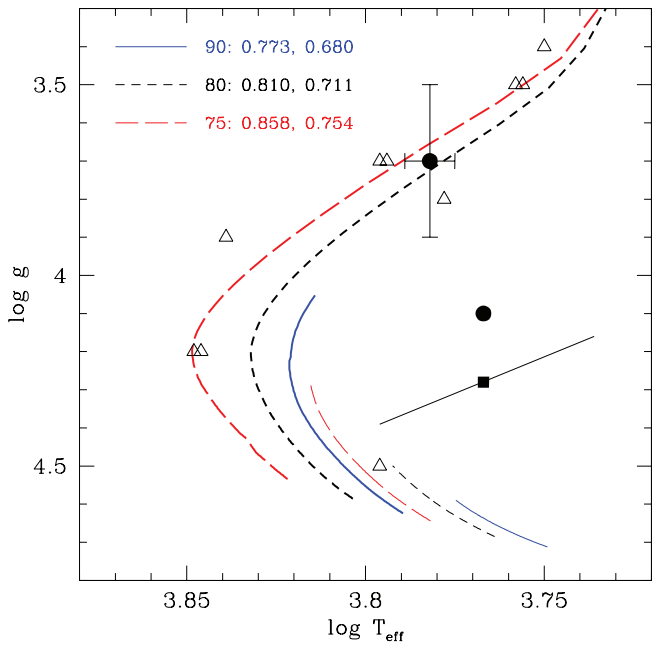

FIG. 5.—Evolutionary tracks (VandenBerg et al. 2006) and CEMP data plotted in the $\log T_{\rm eff}$−$\log g$ plane near the metal-poor main-sequence turnoff. The chosen tracks correspond to three different inclinations of the binary; thick and thin lines are for the primary and secondary, respectively. A full track covers an age range of 4−14 Gyr. The figure legend identifies the masses of the tracks for three different CS 22964−161 orbital sin i choices, using the notation (sin i: M_p, M_s). Filled circles represent the CS 22964−161 primary and secondary ($\log T_{\rm eff}$, $\log g$) values derived from the spectroscopic analysis (§ 5.1). The plotted error bars for the primary are also from the spectroscopy. The square shows the secondary parameters from the dimensional analysis described in § 5.2. The line about this point corresponds to $\Delta T_{\rm eff} = \pm 400$ K. The triangles represent CEMP stars from the literature; see § 5.2 for details. The triangles for three pairs of stars with identical temperatures and gravities have been shifted apart from each other for display purposes.

relationship shown in the figure. Therefore, we computed abundances for a model with parameter set ($T_{\rm eff,s}$, $\log g_s$, $[{\rm M/H}]_s$) = (6300 K, 4.5, −2.2). Assumption of a secondary microturbulent velocity $v_{t,s} = v_{t,p} = -1.2$ km s^{-1} yields ϵ(Fe) = 5.45 and 5.27 from Fe I and Fe II lines, respectively. These values are substantially larger than the mean abundances for primary and secondary given in Table 4, ϵ(Fe) = 5.11. This is in agreement with expectations of a larger derived metallicity from the 350 K increase in $T_{\rm eff,s}$ for this test. However, the Fe I line abundances for this hotter model also exhibit an obvious trend with EW. This problem could be corrected by increasing v_t to 2.4 km s^{-1}, and then we get ϵ(Fe) = 5.18 and 5.15 from Fe I and Fe II lines, respectively, very close to our final adopted Fe abundances for the secondary. However, it is difficult to reconcile such a large v_t with the much smaller value determined with more confidence in the primary, as well as standard values determined in many literature studies of near-turnoff stars.

6. ABUNDANCES OF THE INDIVIDUAL STARS

With the EW data of Table 3 and the interpolated model atmospheres described in § 5, we determined abundances of a few key elements whose absorption lines are detectable in both primary and secondary observed spectra. These abundances are given in Table 4. They suggest that in general the abundance ratios of all elements in the two stars agree to within the stated uncertainties. Both stars are relatively enriched in the α-elements: $\langle$[Mg, Ca, Ti/Fe]$_p\rangle \simeq +0.4$ and $\langle$[Mg, Ca, Ti/Fe]$_s\rangle \simeq +0.3$. Both stars have solar system Ni/Fe ratios, probably no substantial depletions or enhancements of Na (special comment on this element is given in § 7), and large deficiencies of Al. All these abundance ratios are consistent with expectations for normal metal-poor Population II stars.

More importantly, we find very large relative abundances of C, Sr, and Ba ([X/Fe] = +0.5 to +1.5; Table 4) in both primary and secondary stars of the CS 22964−161 system. For Sr and Ba abundances we first used the EW subtraction technique, which suggested roughly equal abundances of these elements in both stars. We confirmed and strengthened this result through synthetic spectrum computations of the strong Sr II $\lambda\lambda$4077.71, 4215.52 and the Ba II λ4554.04 lines in the six velocity-split spectra. To produce the binary syntheses, we modified the MOOG line analysis code to compute individual spectra for primary and secondary stars, then to add them after (1) shifting the secondary spectrum in wavelength to account for the velocity difference between the stars and (2) weighting the primary and secondary spectra by the appropriate luminosity ratio.

In Figure 6 we show the resulting observed/synthetic binary spectrum match for the Sr II λ4077.71 line in observation 13817. The absorption spectrum of the secondary star is shifted by +58.1 km s^{-1} (+0.79 Å), in agreement with the observed feature in Figure 6. The depth of the Sr II line in the secondary is weak, as expected due to the luminosity difference between the two stars ($l_p/l_s \simeq 6$) at this wavelength. Note also in Figure 6 the relative insensitivity of the feature to abundance changes for the secondary, even with the large (±0.5 dex) excursions in its assumed Sr content. This occurs because the Sr II line is as saturated in the secondary as it is in the primary, but the central intensity of the unsmoothed spectrum is ∼0.2 of the continuum. Thus, after the secondary's spectrum is diluted by the much larger flux of the primary, a weak line that is relatively insensitive to abundance changes ensues in the combined spectrum (and a naturally weaker line in the secondary simply becomes undetectable in the sum).

In Figure 7 we illustrate the appearance of a small portion of the CH G-band $A\ ^2\Delta - X\ ^2\Pi^+$ Q-branch band head in the observed combined-light spectra with a large velocity split. This portion of the G band has a sharp blue edge; the central wavelength of the first line is 4323.0 Å. With $\Delta V_R = +58.1$ km s^{-1}, the left edge of the secondary's band head begins at 4323.8 Å, as indicated in the bottom panel of Figure 7. In the top panel we show attempts to match the observed band head with synthetic spectra that include only CH lines of the primary star. When the spectral interval $\lambda < 4324.8$ Å is fitted well, observed absorption is clearly missing at longer wavelengths in the synthetic spectrum. This is completely solved by the addition of the secondary's CH band head, at a comparable C abundance level to that of the primary, as shown in the bottom panel.

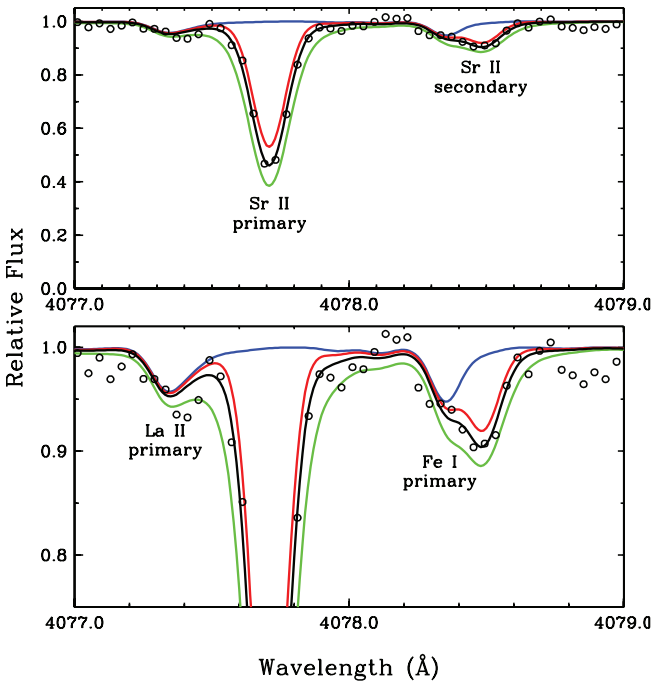

FIG. 6.—Observed and synthetic spectra of the Sr II λ4077.71 line in observation 13817 of CS 22964−161 ($\Delta V_R \simeq 58.09$ km s^{-1}). The top spectrum shows the full relative flux scale, and the bottom spectrum covers just the relative flux region above 0.75. The wavelength scale is at rest velocity for the primary star. The observed spectrum is depicted with open circles. The blue line represents a synthetic spectrum computed without any contribution from Sr. The black line shows the best overall fit to primary and secondary Sr II features: ϵ(Sr) = 0.98 and 0.78, respectively. The red and green lines indicate syntheses for each star that are 0.5 dex smaller and larger, respectively, than the best fits.

It is very difficult to derive reliable abundances in the CS 22964−161 secondary even for the strong features illustrated here. Nevertheless, it is clear that both components of this binary have substantial overabundances of C and n-capture elements Sr and Ba. Within the uncertainties of our analysis, the overabundance factors for these elements appear to be the same. Enhanced C accompanies s-process synthesis of n-capture elements during partial He-burning episodes of low/intermediate-mass stars, and the joint production of these elements is evident in the observed abundances of a number of BMP stars such as CS 29497−030 (Sneden et al. 2003a; Ivans et al. 2005). However, a substantial C overabundance has also been seen in the r-process–rich star CS 22892−052 (Sneden et al. 2003b). The Sr and Ba abundances determined to this point cannot distinguish between possible n-capture mechanisms that created the very heavy elements in CS 22964−161.

7. ABUNDANCES FROM THE SYZYGY SPECTRUM

To gain further insight into the n-capture element abundance distribution, we returned to the higher S/N mean syzygy spectrum.

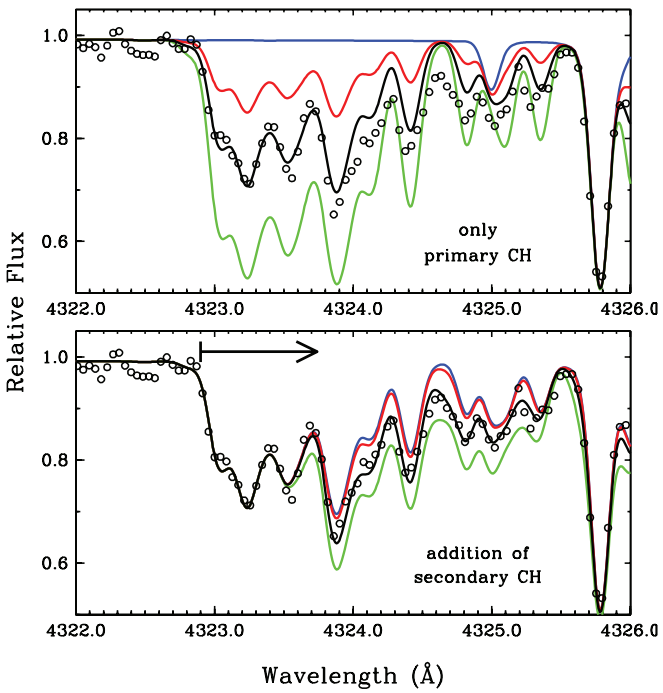

FIG. 7.—Observed and synthetic spectra of the CH G band head in CS 22964−161. The observation is 13817, for which $\Delta V_R = 58.09$ km s^{-1}. Open circles represent the observed spectrum. In the top panel only the contribution of the primary star to this blend is considered. The abundances of the synthetic spectra, in order of increasing CH strength, are $\epsilon(\mathrm{C})_p = -\infty$, 7.24, 7.64, and 8.04 (*blue, red, black, and green lines, respectively*). In the bottom panel, the abundance of the primary is fixed at $\epsilon(\mathrm{C})_p = 7.64$, and that of the secondary is, again in order of increasing CH strength, $\epsilon(\mathrm{C})_s = -\infty$, 6.44, 7.44, and 8.44. An arrow indicates the wavelength offset between primary and secondary stars of this observation.

Preston et al. (2006b) argued that the relative strengths of La II and Eu II lines can easily distinguish *s*-process dominance (stronger La features) from *r*-process dominance (stronger Eu); see their Figure 1. In Figures 8*a* and 8*b* we show the same La and Eu lines discussed by Preston et al. (2006b); the greater strength of the La feature is apparent.

We computed a mean EW from La II lines at 3988.5, 3995.7, 4086.7, and 4123.2 Å and a mean EW from Eu II lines at 3907.1, 4129.7, and 4205.1 Å for a few warm metal-poor stars with *n*-capture overabundances. The resulting ratio $\langle \mathrm{EW_{La}} \rangle / \langle \mathrm{EW_{Eu}} \rangle \simeq 0.5$ for the *r*-process–rich red horizontal branch star CS 22886−043 (Preston et al. 2006a), $\simeq$2.8 for the *s*-process–rich RR Lyrae TY Gruis (Preston et al. 2006a), and $\simeq$2.7 for the *r*+*s* BMP star CS 29497−030 (Ivans et al. 2005). For CS 22964−161 we found $\langle \mathrm{EW_{La}} \rangle / \langle \mathrm{EW_{Eu}} \rangle \simeq 2.7$, an unmistakable signature of an *s*-process abundance distribution.

For a more detailed *n*-capture element distribution for CS 22964−161 we computed synthetic spectra of many transitions in the syzygy spectrum. We used the same binary synthesis version of the MOOG code that was employed for the velocity-split spectra shifted to $\Delta V_R = 0$ km s^{-1} (as described in § 6). For these computations it was also necessary to assume that $\epsilon(\mathrm{X})_p = \epsilon(\mathrm{X})_s$ for all elements X. We also derived abundances of a few lighter elements of interest with this technique. It should be noted that since the primary star is 4–6 times brighter than the secondary, abundances derived in this manner mostly apply to the primary.

In Table 5 we give the abundances for the CS 22964−161 binary system. For elements with abundances determined for the individual stars as discussed in § 6, we also give estimates of their "system" abundances in this table. These mean abundances were computed from the entries in Table 4, giving both the abundances and their uncertainties (σ) of the primary star 5 times more weight than those of the secondary. For elements with abundances derived from synthetic spectra of the syzygy spectrum, the abundances and σ-values are means of the results from individual lines, wherever possible. For several of these elements only one transition was employed. In these cases we adopted $\sigma = 0.20$ or 0.25, depending on the difficulties attendant in the synthetic/observed spectrum matches. In the next few paragraphs we discuss the analyses of a few species that deserve special comment.

Li I.—The resonance transition at 6707.8 Å was easily detected in all CS 22964−161 spectra, with $\mathrm{EW}_{o,\mathrm{tot}} \simeq 24.5$ mÅ from the syzygy data. Our synthesis included only ^{7}Li, but with its full hyperfine components. The resolution and S/N combination of our spectra precluded any meaningful search for the presence of ^{6}Li. Reyniers et al. (2002) have shown that the presence of a Ce II transition at 6708.09 Å can substantially contaminate the Li feature in *n*-capture–rich stars. However, in our spectra the Ce line wavelength is too far from the observed feature, and our syntheses indicated that the Ce abundance would need to be about 2 orders of magnitude larger than our derived value (Table 5) to produce measurable absorption in the CS 22964−161 spectrum.

We attempted to detect the secondary Li I line in two different ways. First, we applied the subtraction technique (§ 4) to this feature. However, the six velocity-split spectra yielded $\mathrm{EW}_{o,p} = 23.5$ mÅ with $\sigma = 3.5$ mÅ (consistent with typical uncertainties for this technique). Thus, the implied $\mathrm{EW}_{o,s} = 1.0$ mÅ is consistent with no detection of the secondary's line. Second, we coadded the velocity-split spectra after shifting them to the rest system of the secondary. A very weak ($\mathrm{EW}_{o,s} \simeq 4$ mÅ) line appears at $\lambda = 6707.9$ Å, about 0.1 Å redward of the Li I feature centroid. We computed synthetic spectra assuming that the observed line is Li, and we derived $\epsilon(\mathrm{Li}) \simeq +2.0$ with an estimated uncertainty of ± 0.2 from the observed/synthetic fit. This abundance is fortuitously close to the system value, but we do not believe that the present data warrant a claim of Li detection in the CS 22964−161 secondary.

Na I.—The $\lambda\lambda$5682, 5688 doublet, used in abundance analyses when the D lines at 5890 and 5896 Å are too strong, is undetectably weak in CS 22964−161. A synthetic spectrum match to the syzygy spectrum suggests that $\epsilon(\mathrm{Na}) \lesssim 3.9$. The D lines are strong, $\sim$40% deep. Unfortunately, their profiles appear to be contaminated by telluric emission. If we assume that the line centers and red profiles are unblended, then $\epsilon(\mathrm{Na}) \simeq 3.9$.

Given the great strengths of the D lines in the syzygy spectrum (dominated by the primary star), we returned to the velocity-split spectra and searched for the secondary Na D lines. Absorptions a few percent deep at the expected wavelengths were seen in all spectra. Co-addition of these spectra after shifting to the rest velocity system of secondary yielded detection of both D lines, and we estimated $\epsilon(\mathrm{Na}) \simeq 3.8$. A problem with our analyses of the D lines in all spectra was the lack of telluric H_2O line cancellation; we did not observe suitable hot, rapidly rotating stars for this purpose. However, any unaccounted-for telluric features would drive the derived Na abundances to larger values. Thus, we feel confident that Na is not overabundant in CS 22964−161.

CH.—Carbon was determined from CH G-band features in the wavelength range 4260–4330 Å, with a large number of individual lines contributing to the average abundance. Our CH line list was taken from the Kurucz (1998) compendium. The solar C abundance listed in Table 5 was determined with the same line list (see Sneden et al. 2003a), rather than adopted from the recent revision of its abundance from other spectral features by Allende Prieto et al. (2002).

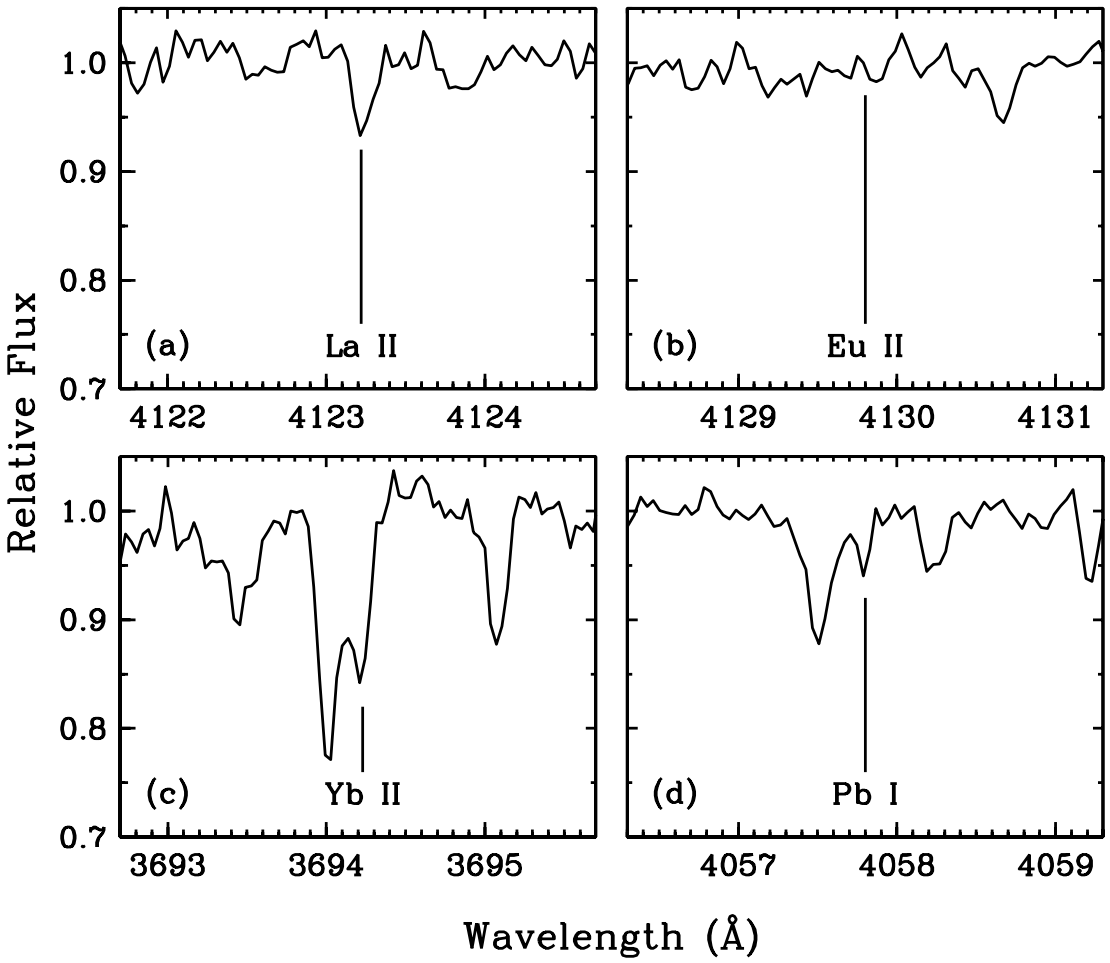

FIG. 8.—Selected spectral features of *n*-capture species in the CS 22964−161 syzygy spectrum.

Si I.—The only detectable line, at 3905.53 Å, suffers potentially large CH contamination, as pointed out by, e.g., Cohen et al. (2004). These CH lines are very weak in ordinary warm metal-poor stars (Preston et al. 2006a) but are strong in C-enhanced CS 22964−161. We took full account of the CH in our synthesis of the Si I line. Note that the secondary's Si I line can be detected in the velocity-split spectra, but it is always too blended with primary CH lines to permit a useful primary/secondary Si abundance analysis.

Species with substructure.—Lines of Sc II, Mn I, Y II, and La II have significant hyperfine subcomponents, which were explicitly accounted for in our syntheses (each of these elements has only one naturally occurring isotope). For Ba II and Yb II (whose single spectral feature at 3694.2 Å is shown in Fig. 8*c*), both hyperfine and isotopic substructures were included. We assumed an *s*-process distribution of their isotopic fractions: $f(^{134}\mathrm{Ba}) = 0.038$, $f(^{135}\mathrm{Ba}) = 0.015$, $f(^{136}\mathrm{Ba}) = 0.107$, $f(^{137}\mathrm{Ba}) = 0.080$, $f(^{138}\mathrm{Ba}) = 0.758$; and $f(^{171}\mathrm{Yb}) = 0.180$, $f(^{172}\mathrm{Yb}) = 0.219$, $f(^{173}\mathrm{Yb}) = 0.191$, $f(^{174}\mathrm{Yb}) = 0.226$, $f(^{176}\mathrm{Yb}) = 0.185$. We justify the *s*-process mixture choice below by showing that the total abundance distribution, involving 17 elements, follows an *s*-process–dominant pattern.

Pb I.—The λ4057.8 line was easily detected in the syzygy spectrum (Fig. 8*d*), with $\mathrm{EW}_{o,\mathrm{tot}} \sim 5$ mÅ. This line is very weak, but we confirmed its existence and approximate strength through co-addition of the six velocity-split spectra. The Pb abundance was derived from synthetic spectra in which the isotopic and hyperfine substructures were taken into account following Aoki et al. (2002) and using the Pb I line data of their Table 4. Variations in assumed Pb isotopic fractions produced no change in the derived elemental abundance. As with other features in the blue spectral region, CH contamination exists, but our syntheses suggested that it is only a small fraction of the Pb I strength.

8. IMPLICATIONS OF THE CS 22964−161 ABUNDANCE PATTERN

In the top panel of Figure 9 we plot the abundances relative to solar values for the 10 *n*-capture elements detected in the CS 22964−161 syzygy spectrum, together with the *n*-capture abundances in the very *s*-process–rich BMP star CS 29497−030. These two stars have nearly the same overall [Fe/H] metallicity, as indicated by the horizontal lines in the panel. The *n*-capture overabundance pattern of CS 22964−161 clearly identifies it as another member of the C- and *s*-process–rich "lead star" family.

However, the relative *n*-capture abundance enhancements [X/Fe] of CS 29497−030 are about 1 dex higher than they are in CS 22964−161. This is emphasized by taking the difference between the two abundance sets, as is displayed in the bottom panel of Figure 9. These differences illustrate the trend toward weaker *s*-process enhancements of the heaviest elements in CS 22964−161 compared to CS 29497−030.

Many studies have argued that these overall abundance anomalies, now seen in many low-metallicity stars, must have originated from mass transfer from a (former) AGB companion to the stars observed today. Whole classes of stars with large C and *s*-process abundances are dominated by single-line spectroscopic

TABLE 5
ABUNDANCE FOR THE CS 22964−161 SYSTEM

Species	$\log \epsilon_\odot$	$\log \epsilon$	σ	No.	[X/H]	[X/Fe]	Method[a]
Fe I	7.52	+5.13	0.21	104	−2.39	+0.02	est
Fe II	7.52	+5.09	0.17	7	−2.43	−0.02	est
Li I.....	...	+2.09	0.20	1	...	...	est
CH.....	8.70	+7.50	0.15	1	−1.20	+1.21	syn
Na I.....	6.33	+3.9	0.3	4	−2.4	0.0	syn
Mg I.....	7.58	+5.53	0.20	6	−2.05	+0.36	syn
Al I	6.57	+3.26	0.20	1	−3.31	−0.90	est
Si I.....	7.55	+5.28	0.25	1	−2.27	+0.14	syn
Ca I.....	6.36	+4.32	0.16	8	−2.04	+0.37	est
Ti II.....	4.99	+3.18	0.34	9	−1.81	+0.60	est
Cr I	5.64	+3.27	0.34	8	−2.37	+0.04	est
Cr II	5.64	+3.48	0.12	2	−2.16	+0.25	est
Mn I.....	5.39	+2.27	0.15	3	−3.12	−0.71	syn
Ni I	6.25	+3.91	0.30	10	−2.34	+0.07	est
Sr II.....	2.90	+1.01	0.11	2	−1.89	+0.52	syn
Y II	2.24	+0.12	0.10	3	−2.12	+0.29	syn
Zr II.....	2.60	+0.88	0.25	1	−1.72	+0.69	syn
Ba II.....	2.13	+0.98	0.16	5	−1.15	+1.26	syn
La II	1.13	−0.21	0.10	4	−1.34	+1.07	syn
Ce II.....	1.55	+0.43	0.25	1	−1.12	+1.29	syn
Nd II	1.45	+0.05	0.12	3	−1.40	+1.01	syn
Eu II.....	0.52	−1.20	0.26	5	−1.72	+0.69	syn
Yb II	1.08	−0.69	0.25	1	−1.77	+0.64	syn
Pb I.....	1.85	+1.63	0.20	1	−0.22	+2.19	syn

[a] Abundance method: "est" means that the system abundance was estimated from the individual primary and secondary abundances given in Table 4; "syn" means that the system abundance was computed with synthetic spectra of features in the syzygy spectrum.

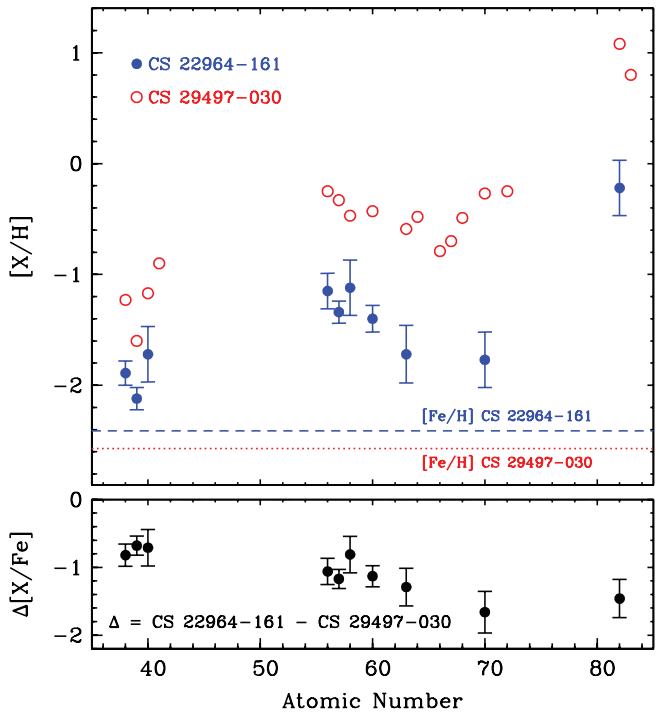

FIG. 9.—*Top*: *n*-capture abundances relative to solar values [X/H] from the CS 22964−161 combined spectrum plotted along with those of the BMP very *s*-process−rich star CS 29497−030 (Ivans et al. 2005). Horizontal lines are drawn to indicate the general Fe metallicity levels of the two stars. *Bottom*: Abundance differences between these two stars.

binaries, including the high-metallicity "Ba II stars" (McClure et al. 1980; McWilliam 1988; McClure & Woodsworth 1990), the low-metallicity red giant "CH stars" (McClure 1984), the "subgiant CH stars" (McClure 1997), and the BMP stars (Preston & Sneden 2000; note that not all BMP stars share these abundance characteristics). The case is especially strong for the subgiant CH and BMP stars, for these are much too unevolved to have synthesized C and *s*-process elements in their interiors and dredged these fusion products to the surfaces. Our analysis has confirmed that primary and secondary CS 22964−161 stars are on or near the main sequence. Therefore, we suggest that a third, higher mass star is now or once was a member of the CS 22964−161 system. During the AGB evolutionary phase of the third star, it transferred portions of its C- and *s*-process−rich envelope to the stars we now observe.

The very large Pb abundance of CS 22964−161 strengthens the AGB nucleosynthesis argument. Gallino et al. (1998) and Travaglio et al. (2001) predicted substantial Pb production in *s*-process fusion zones of metal-poor AGB stars. In metal-poor stars, the neutron-to-seed ratio is quite high, permitting the *n*-capture process to run through to Pb and Bi, the heaviest stable elements along the *s*-process path. Prior to this theoretical prediction, it was assumed that a *strong* component of the *s*-process was required for the manufacture of half of the ^{208}Pb in the solar system (Clayton & Rassbach 1967). That the patterns of the abundances of the *n*-capture elements in CS 22964−161 and CS 29497−030 resemble each other so well is a reflection of how easily low-metallicity AGB stars can synthesize the heavy elements.

8.1. *Inferred Nucleosynthetic and Dilution History*

We explored the origin of the *n*-capture enhancements in CS 22964−161 by comparing the derived photospheric abundances with predicted stellar yields from the *s*-process. Employing FRANEC stellar evolutionary computations (see Straniero et al. 2003, 2006), we performed nucleosynthetic calculations following those of Gallino et al. (1998, 2006b) and Bisterzo et al. (2006). We then sought out good matches between the observed and predicted abundance pattern distributions with low-mass AGB progenitors of comparable metallicities and a range of initial masses.

We employed AGB models adopting different ^{13}C pocket efficiencies and initial masses to explore the nucleosynthetic history of the observed chemical compositions (Busso et al. 1999; Straniero et al. 2003). Permitting some mixing of material between the *s*-process−rich contributions of the AGB donor and the H-rich material of the atmosphere in which the contributions were deposited, we identified those AGB model progenitors that would yield acceptable fits for the predicted yields of all *s*-process elements beyond Sr.

Ascertaining the best matches between the observed and predicted yields was performed in the following way. For a given initial AGB mass, we inspected the abundances of [Zr/Fe], [La/Fe], and [Pb/Fe] for various ^{13}C pocket efficiencies adopted in the calculations. The difference between our predicted [La/Fe] and that of the observed abundance ratio gave us a first guess to the dilution of material for a given ^{13}C pocket efficiency. The dilution factor (dil) is defined as the logarithmic ratio of the mass of the envelope of the observed star polluted with AGB stellar winds and the AGB total mass transferred: dil $\equiv \log (M_{\rm obs}^{\rm env}/M_{\rm transf}^{\rm AGB})$. The ^{13}C pocket efficiency is defined in terms of the ^{13}C pocket mass involved in an AGB pulse that was adopted by Gallino et al. (1998). Their § 2.2 states, "The mass of the ^{13}C pocket is $5.0 \times 10^{-4}\ M_\odot$ [here called ST], about 1/20 of the typical mass involved in a thermal pulse. It contains $2.8 \times 10^{-6}\ M_\odot$ of ^{13}C." Thus, our shorthand notation for ^{13}C pocket efficiency will be ST/N, where "N" is the reduction factor employed in generating a particular set of

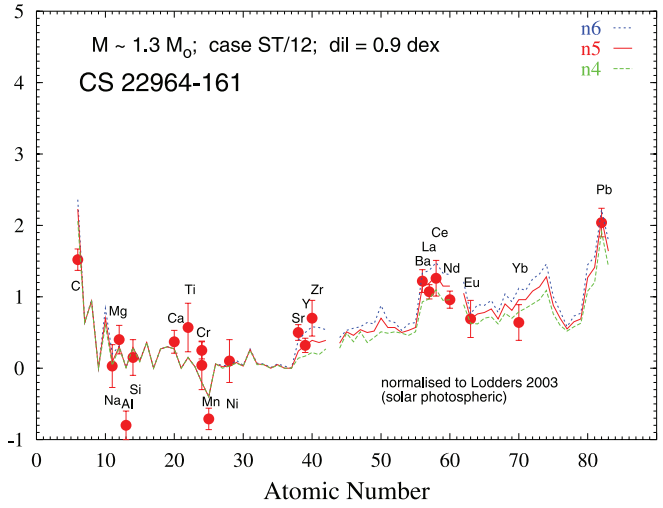

FIG. 10.—Comparison of the [X/Fe] abundances in CS 22964−161 with predictions from *s*-process calculations of a 1.3 $M_\odot$ AGB star model. The solid red line corresponds to the best match between the observed and predicted abundance pattern. The dotted blue and dashed green lines indicate the difference that adopting models of $\pm 0.05\ M_\odot$ would make (effectively, changing the number of thermal pulses from 4 to 6, identified in the figure legend as n4, n5, n6). For the specific choice of the ^{13}C pocket (ST/12), and for the definition of the dilution factor (dil), see § 8.1.

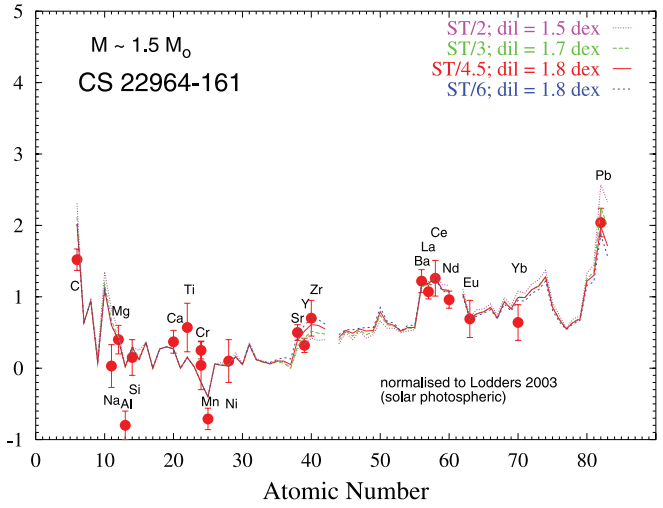

FIG. 11.—Comparison of the [X/Fe] abundances in CS 22964−161 with predictions from *s*-process calculations of a 1.5 $M_\odot$ AGB star model. The solid red line corresponds to the best match between the observed and predicted abundance pattern. The dotted magenta, long-dashed green, and short-dashed blue lines show the difference made to the pattern by adopting different amounts of dilution. For discussion of the various choices of the ^{13}C pocket efficiency (ST/N) and the dilution factor (dil), see § 8.1.

AGB abundance predictions. Subtracting this dilution amount from the predicted [Pb/Fe], we then compared the result to the observed [Pb/Fe]. The large range of ^{13}C pocket efficiencies was then narrowed down, keeping only those results that fit the abundances of both [La/Fe] and [Pb/Fe] within 0.2 dex. Similar iterations were performed employing the abundances of [Zr/Fe].

We repeated this process for a range of initial AGB mass choices: 1.3, 1.5, 2, 3, and 5 $M_\odot$. For AGB models of initial mass 3 and 5 $M_\odot$ no good match was found because the light *s*-elements (ls ≡ Sr, Y, Zr) were predicted to have too high abundances with respect to the heavy *s*-elements (hs ≡ Ba, La, Ce, Nd). For AGB models of $M \leq 2\ M_\odot$ a satisfactory solution was found for ls, hs, and Pb, provided that a proper ^{13}C pocket efficiency and dilution factor were chosen. In Figures 10 and 11 we show the matches between predicted and observed abundances for the two lowest mass models, 1.3 and 1.5 $M_\odot$, respectively.

The abundances of the light elements Na and Mg further narrowed the range of allowable AGB progenitor models. Two independent channels are responsible for creating ^{23}Na: the ^{22}Ne(p, γ)^{23}Na reaction during H shell burning, and the neutron capture on ^{22}Ne via the chain ^{22}Ne(n, γ)^{23}Ne($\beta^-\nu$)^{23}Na in the convective He flash (see Mowlavi 1999; Gallino et al. 2006a). A large abundance of primary ^{22}Ne derives from the primary ^{12}C mixed with the envelope by previous third dredge-up episodes, then converted to primary ^{14}N by HCNO burning in the H-burning shell and followed by double α capture via the chain ^{14}N(α, γ)^{18}F($\beta^+\nu$)^{18}O(α, γ)^{22}Ne during the early development of the convective thermal pulse. The next third dredge-up episode mixes part of this primary ^{22}Ne with the envelope. Finally, while the H-burning shell advances in mass, all the ^{22}Ne present in the H shell is converted to ^{23}Na by proton capture, accumulating in the upper region of He intershell. Note that in intermediate-mass AGB stars suffering the so-called hot bottom burning (HBB) in the deeper layers of their convective envelope, efficient production of ^{23}Na results from proton capture on ^{22}Ne (Karakas & Lattanzio 2003). Furthermore, the marginal activation in the convective He flash of the reactions ^{22}Ne(α, n)^{25}Mg and ^{22}Ne(α, γ)^{26}Mg would lead to enhanced Mg. At the same time, most neutrons released by ^{22}Ne(α, n)^{25}Mg are captured by the very abundant primary ^{22}Ne, thus producing ^{23}Na through the second channel indicated above.

Comparison of the abundance data in Figures 10 and 11 shows that the observed [Na/Fe] argues for the exclusion of the 1.5 $M_\odot$ AGB model, which overpredicts this abundance ratio by ~0.5 dex. The same statement applies to the 2 $M_\odot$ model, not illustrated here. The larger Na abundances produced in these models, relative to the 1.3 $M_\odot$ model, are related to the larger number of thermal pulses (followed by third dredge-up) that these stars experience. These arguments leave the 1.3 $M_\odot$ AGB model as the only one capable of providing a global good match to all observed elements.

In order to match these abundances, the predicted AGB yields require an inferred dilution by H-rich material. We do not know the distance between the AGB primary donor and the low-mass companion (actually, the binary system) that is now observed. We also do not know precisely the mass loss rate of the AGB. Dilution by about 1 dex of *s*-process–rich AGB material with the original composition of the observed star, as we deduce on the basis of the above nucleosynthesis analysis, only fixes the ratio of the accreted matter with the outer envelope of the observed star. A more detailed discussion is taken up in § 8.2.

A final remark concerns C, for which Figures 10 and 11 indicate a ~0.8 dex overproduction compared to the observed [C/Fe]. This mismatch can in principle be substantially reduced by the occurrence of the so-called cool bottom process (CBP; see Nollett et al. 2003; Domínguez et al. 2004a, 2004b). This reduction would imply a substantial increase of predicted N abundance, from [N/Fe] ~ +0.5, shown in Figures 10 and 11, to perhaps +1.5. We attempted without success to detect the strongest CN absorption at the 3883 Å band head. Trial spectral syntheses of this wavelength region suggested that even [N/Fe] ~ +1.5 would not produce detectable CN.

8.2. *Mixing and Dilution in the Stellar Outer Layers*

Very recently Stancliffe et al. (2007), extending the earlier discussion of Theuns et al. (1996), report that extensive mixing due to thermohaline instability in a metal-poor star on the main sequence

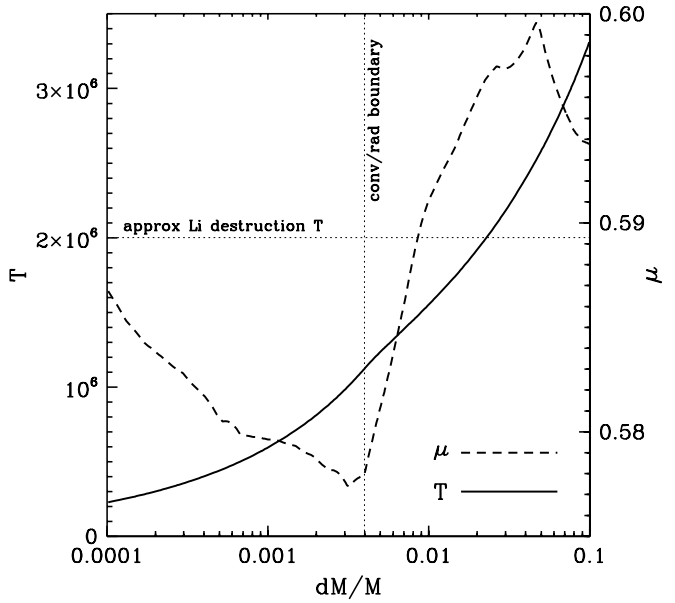

FIG. 12.—Mean molecular weight (μ) and temperature (T) profiles, as functions of the fractional mass (mass above the considered layer), in a 0.78 $M_\odot$ star with [Fe/H] = −2.3, at an age of 3.75 Gyr. Here μ is the real molecular weight, including partial ionization. The fractional mass of the convective zone is 0.004. The helium depletion due to gravitational settling, of about 20% in this case, already leads to an important stabilizing μ-gradient below the convective zone. This model is one of those computed by Richard et al. (2002), including pure atomic diffusion. The full model was made available to us by O. Richard (2007, private communication).

may severely dilute material that has been accreted from a companion. They computed the mixing timescale with the assumption that thermohaline convection behaved as a simple diffusion process, and they concluded that the new matter should rapidly be mixed down over about 90% of the stellar mass.

Treating thermohaline convection simply as diffusion does not take into account the special nature of this process, which has extensively been studied in oceanography (e.g., Veronis 1965; Kato 1966; Turner 1973; Turner & Veronis 2000; Gargett & Ruddick 2003) and has also been considered in stars (Gough & Toomre 1982; Vauclair 2004). Thermohaline convection occurs in the ocean when warm salty water comes on top of cool fresh water. In this case the stabilizing thermal gradient acts against the destabilizing salt gradient. If the stabilizing effect compensates the destabilizing one, the medium should be stable, but it remains unstable due to double diffusion: when a blob begins to fall down, heat diffuses out of it more rapidly than salt; then the blob goes on falling as the two effects no longer compensate. This creates the well-known "salt fingers" and thus is a very different physical environment than ordinary convection.

A similar situation occurs in stars when high-μ matter comes on a lower μ region, which is the case for hydrogen-poor accretion. This has been studied in detail for the case of planetary accretion on solar-type stars (Vauclair 2004). As shown in laboratory experiments (Gargett & Ruddick 2003), the fingers develop in a special layer with a depth related to the velocity of the blobs and to the dissipation induced by hydrodynamical instabilities at their edges. This is a complicated process that may also be perturbed by other competing hydrodynamical effects. Depending on the situation, it is possible that the "finger" regime stops before complete mixing of the high-μ material into the low-μ one. In this case, we expect that the final amount of matter that remains in the thin subphotospheric convective zone depends only on the final μ-gradient, whatever the original amount accreted: more accreted matter leads to more mixing so that the final result is the same.

TABLE 6
PREDICTED MASS FRACTION AND MOLECULAR WEIGHT

Mass Fraction	$M = 1.3\ M_\odot$	$M = 1.5\ M_\odot$
At Last Third Dredge-up		
X	0.675	0.535
Y	0.301	0.403
Z	0.0238	0.062
μ	0.630	0.713
Mass Average of the Winds		
X	0.700	0.585
Y	0.284	0.367
Z	0.0155	0.0483
μ	0.616	0.781

Another very important point has to be mentioned. At the epoch when accretion occurs on the dwarfs, these stars are already about 3–4 Gyr old. Gravitational settling of helium and heavy elements has already occurred and created a stabilizing μ-gradient below the convective zone (Vauclair 1999; Richard et al. 2002). For example, as we illustrate in Figure 12, in a 0.78 $M_\odot$ star with [Fe/H] = −2.3, after 3.75 Gyr the μ-value is as low as 0.58 inside the convective zone while it goes up to nearly 0.60 in deeper layers. Thus, the stabilizing $\Delta\mu/\mu$ is already of order 0.02. If the star accretes hydrogen-poor matter, thermohaline convection may begin, but it remains confined by the μ-barrier. The star can accrete as much high-μ matter as possible until this stabilizing μ-gradient is flattened.

In § 8.1 we saw, from the observed abundances and the AGB nucleosynthetic computations, that the dilution factor is of the order of 1 dex for the AGB model of initial mass ∼1.3 $M_\odot$. Table 6 lists the predicted mass fraction of hydrogen (X), helium (Y), and heavier elements (Z) in the envelope of AGB progenitor stars of 1.3 and 1.5 $M_\odot$ for two cases. The first case describes the final abundance mix produced by the AGB at the end of its nucleosynthetic lifetime (the last third dredge-up). The second case describes the mass average of the winds from the AGB over its *s*-processing lifetime. Also noted is the mean molecular weight of the material (μ), assuming fully ionized conditions. From Table 6, the μ-value in the wind lies in the range 0.61–0.78. From these computations, we find that, after dilution, the μ-value inside the convective zone should increase by $\Delta\mu/\mu \simeq 0.1\%$–4%. Clearly most of the inferred values for the dilution factor are compatible with stellar physics. For the lowest values it is possible that the accreted matter simply compensates the effect of gravitational diffusion. For larger values, thermohaline convection can have larger effects, but, following Vauclair (2004), if we accept an inverse μ-gradient of order $\Delta\mu/\mu = 0.02$ below the convective zone, such an accreted amount would still be possible.

8.3. *The Extraordinary Abundance of Lithium*

Near main-sequence turnoff CEMP stars display a variety of Li abundances. The majority have undetectable Li I λ6708 lines, implying $\epsilon(\mathrm{Li}) < +1$. A few have abundances similar to the Spite & Spite (1982) plateau: $\epsilon(\mathrm{Li}) = +2.10 \pm 0.09$ (Bonifacio et al. 2007). These include our CEMP binary CS 22964−161 and at least CS 22898−027 (Thorburn & Beers 1992) and LP 706-7 (Norris et al. 1997). A few more stars have Li abundances somewhat less than the Spite plateau value, e.g., $\epsilon(\mathrm{Li}) \simeq +1.7$ in CS 31080−095 and CS 29528−041 (Sivarani et al. 2006). This CEMP Li abundance variety stands in sharp contrast to the nearly constant

value exhibited by almost all normal metal-poor stars near the main-sequence turnoff region.

Although CS 22964−161 has a Spite plateau Li abundance, it is unlikely that this is the same Li with which the system was born. Considering just the primary star, suppose that the C and *s*-process–rich material that it received was Li-free. If this material simply blanketed the surface of the primary, mixing only with the original Li-rich atmosphere and outer envelope skin, then the resulting observed Li would be at least less than the plateau value. Alternatively, if the transferred material induced more significant mixing of the stellar envelope, the surface Li would be severely diluted below the limit of detectability in the primary's atmosphere. In order to produce the large observed Li abundance in the primary, freshly minted Li must have been transferred from the AGB donor star.

Li can be produced during the AGB phase both in massive AGB stars and in low-mass AGB stars via $^3\mathrm{He}(\alpha,\gamma)^7\mathrm{Be}(e^-,\nu_e)^7\mathrm{Li}$, but hot protons rapidly destroy it via $^7\mathrm{Li}(p,\alpha)^4\mathrm{He}$. Cameron & Fowler (1971) proposed that in some circumstances the freshly minted ^{7}Be can, however, be transported to cooler interior regions before decaying to ^{7}Li. In massive AGB stars ($4\ M_\odot \lesssim M \lesssim 7\ M_\odot$) nucleosynthesis at the base of the convective envelope (HBB; Scalo et al. 1974) can produce abundances via the Cameron-Fowler mechanism as high as $\log \epsilon(^7\mathrm{Li}) \sim 4.5$ (Sackmann & Boothroyd 1992). However, the lifetimes of these massive AGB stars are far too short to be considered as a likely source of Li in CS 22964−161.

In models of low-mass AGB stars ($1\ M_\odot \leq M \leq 3\ M_\odot$) of $[\mathrm{Fe/H}] = -2.7$, Iwamoto et al. (2004) find that an H-flash episode can occur subsequent to the first fully developed He shell flash. The convection produced by the He shell flash in this metal-poor star model can reach the bottom of the overlying H layer and bring protons down into the He intershell region, a region hot enough to induce an H flash. The high-temperature conditions of the H flash can then produce ^{7}Li by the Cameron-Fowler mechanism. Although the Iwamoto et al. (2004) $2.5\ M_\odot$ model produced a weak H flash, the less massive models produced more energetic ones. In the lowest mass models, surface abundances of $\log \epsilon(^7\mathrm{Li}) > 3.2$ were achieved. Note that there is a maximum metallicity close to $[\mathrm{Fe/H}] = -2.5$ beyond which such an H flash is not effective at producing ^{7}Li. Another viable mechanism for producing a very high abundance of ^{7}Li in low-mass AGB stars of higher metallicities, as observed in the intrinsic C(N) star Draco 461 ($[\mathrm{Fe/H}] = -2.0 \pm 0.2$), was advanced by Domínguez et al. (2004a, 2004b) and is based on the operation of the CBP introduced in § 8.1.

Although *s*-process calculations were not performed in the Iwamoto et al. (2004) study, we note that it would seem that the parameters of the best-fit model of § 8.1 would produce sufficient Li to fit the observations of CS 22964−161.

9. IMPLICATIONS FOR THE PUTATIVE AGB DONOR STAR

The binary nature of CS 22964−161 presents a unique opportunity to explore the nature of the AGB star presumably responsible for its abundance anomalies. The ingredients of the exploration are (1) the analysis of our radial velocities of CS 22964−161 obtained over an interval of about 1100 days, (2) estimation of the orbit changes caused by accretion from an AGB companion, (3) stability of the hierarchical triple system in its initial and final states (Donnison & Mikulskis 1992, hereafter DM92; Szebehely & Zare 1977; Tokovinin 1997; Kiseleva et al. 1994), and (4) application of an appropriate initial-final mass relation for stars of intermediate mass (Weidemann 2000 and references therein).

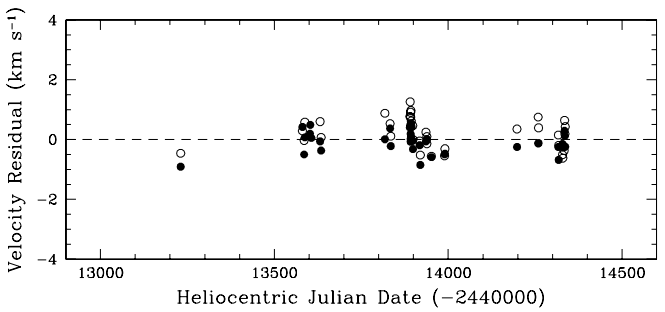

FIG. 13.— Velocity residuals to the fitted orbit plotted against the date of observation for the Magellan data. Filled circles represent the primary, and open circles represent the secondary. These residuals show no trend with time.

9.1. *Evidence for an AGB Relic?*

Velocity residuals calculated for our orbit solution show no trend with time over the nearly 1100 day interval of observation. This is illustrated by the plot of orbital velocity residuals versus Julian Date in Figure 13. Thus, we have yet to find evidence for a third component in the system. The Julian Date interval of our CS 22964−161 data is modest compared to the longest orbital periods of the so-called Barium and CH giant stars (McClure & Woodsworth 1990) and main-sequence/subgiant CH stars (McClure 1997) summarized in Table 7. On the other hand, the errors of our observations ($\sigma = 0.5$ km s^{-1}) are small compared to typical velocity semiamplitudes of these comparison C-rich stellar samples, so drift of the center-of-mass velocity by as much as 1 km s^{-1} due to the presence of a third star should be detectable. Accordingly, Figure 13 encourages us to contemplate the possibility that CS 22964−161 is not accompanied by a white dwarf relic of AGB evolution. Continuing observation will be required to test this notion.

9.2. *Change in Orbit Dimensions Induced by Accretion*

The consequences of mass accretion by a binary were first explored by Huang (1956), who calculated the change in semimajor axis of a binary embedded in a stationary interstellar cloud. Using McCrea's (1953) "retarding force" that followed from Bondi-Hoyle-Lyttleton accretion theory (Bondi & Hoyle 1944), Huang found that mass accretion shrinks orbits, and he proposed that this process could produce close binaries. The problem of binary accretion has been revisited in recent years by numerical simulations of star formation in molecular clouds. Bate & Bonnell (1997) calculate the changes in binary separation due to accretion by an infalling circumstellar cloud. The change is very sensitive to the assumed specific angular momentum (SAM) carried by the accreted material. In the case of low SAM they recover Huang's result. For large SAM orbits the binaries expand. More recently Soker (2004) has calculated the SAM of mass accreted by a binary system embedded in the wind of an AGB star, which is our case. For triple systems containing a distant AGB companion with approximately coplanar inner and outer orbital orbits (statistically most probable in the absence of a special orientation mechanism) he also recovers Huang's result. Finally, building on an earlier analysis by Davies & Pringle (1980), Livio et al. (1986) found that the rate of accretion of angular momentum from winds is significantly less than that deposited in the simple Bondi-Hoyle accretion model.

Our gloss on all these analyses is that the most likely consequence of mass transfer to CS 22964−161 from its AGB companion a long time ago was a decrease in separation; i.e., the initial separation was larger than its present value of ∼0.9 AU.

TABLE 7
Carbon-rich Star Periods and Velocity Ranges

Group	P[a] Range (days)	Median P (days)	K[b] Range (km s^{-1})	Median K (km s^{-1})
Barium-CH giant.....	80–4390	1352	2.5–12.0	6.0
CH subgiant.....	880–4140	1930	3.3–7.2	4.6

[a] Orbital period.
[b] Velocity semiamplitude.

Conservatively, we use 0.9 AU as a lower limit in the estimates that follow below.

Empirical stability criteria for hierarchical triple systems are expressed as the ratio of the semimajor axis of the outer orbit to the semimajor axis of the inner orbit (Heintz 1978, p. 66; Szebehely & Zare 1977), and alternatively as the ratio of periods of the outer and inner orbits (Kiseleva et al. 1994; Tokovinin 1997). If these ratios exceed critical values, a triple system can be long lived. Note, however, the cautionary remarks of Szebehely & Zare (1977) about the role of component masses in evaluation of stability for particular cases and the relevance of these masses to the conclusions of DM92 about the fate of our AGB relic.

Let a_{12} be the semimajor axis of the relative orbit of CS 22964−161 and a_3 be the relative semimajor axis that joins the center of mass of CS 22964−161 to the third (AGB-to-be) star. If we accept the Heintz (1978) and Szebehely & Zare (1977) stability criterion $a_3/a_{12} > 8$, then $a_3 > 7.3$ AU and the orbital period of the outer binary had to be $P > 4000$ days. For Tokovinin's (1997) more permissive criterion, $P_3/P_{12} > 10$, the minimum period is $P > 2500$ days and $a_3/a_{12} > 4.6$. Under these conditions none of our candidate metal-poor AGB stars (see the discussion in § 8.1) with $M < 2\ M_\odot$ fill the Roche lobes (Marigo & Girardi 2007) of these minimum orbits, so wind accretion must have been the mechanism of mass transfer. According to Theuns et al. (1996), a 3 $M_\odot$ AGB star in a 3 AU circular orbit will transfer no more than ∼1% of its wind mass to a 1.5 $M_\odot$ companion by wind accretion. Applying their result to our case, $M(\mathrm{AGB}) \leq 1.5\ M_\odot$ and AGB relic mass ∼0.5 $M_\odot$, the maximum mass transfer is about $(1.5 - 0.5) \times 0.015 \simeq 0.015\ M_\odot$.

The remainder of the AGB wind mass is ejected from the system. We calculated the change in period and semimajor axis of the AGB orbit following Hilditch (2001, p. 164) for the case of a spherically symmetric wind. The orbit expands and the period lengthens according to $\ln(a_f/a_i) = \ln(1+u_i) - \ln(1+u_f)$ and

$$\ln\left(P_f/P_i\right) = 2\ln(1+u_i) - 2\ln\left(1+u_f\right),$$

in which initial and final values of u are $u_i = M_{3i}/(M_1+M_2)$ and $u_f = M_{3f}/(M_1+M_2)$. We have ignored small changes in M_1 and M_2. For $M_3 = 1.3\ M_\odot$ and the Tokovinin (1997) stability condition ($a_3/a_{12} > 4.6$), the minimum orbit expands from 4.2 to 5.9 AU and the minimum period lengthens from 1900 to 3700 days. For the more restrictive Heintz ($a_3/a_{12} > 8$) stability condition the minimum orbit expands from 7.3 to 10.2 AU and the minimum period lengthens from 4300 to 8400 days. The K-values for the center of mass of the CS 22964−161 binary for the two cases are 4.3 and 3.3 km s^{-1}, respectively, both readily detectable by conventional echelle spectroscopy.

9.3. *Dynamical Stability of CS 22964−161 as a Hierarchical Triple System*

The DM92 study investigated the stability of triple systems that consist of a close inner binary with masses (M_1, M_2) and semimajor axis $a1$ attended by a remote companion of mass M_3 at distance $q2$ from the center of mass of the inner binary. They use the parameter notation of Harrington's (1975) pioneering numerical simulations. DM92 investigate stability in three mass regimes, by integration of the equations of motion for various sets of masses, initial positions, and velocities: (1) $M_3 \leq$ minimum(M_1, M_2), (2) $M_1 \geq M_3 \geq M_2$, and (3) $M_3 \geq$ maximum(M_1, M_2). They pursued the integrations for at least 1000 orbits of the inner binary or until disruption, which ever happened first. Among the several results in § 5 of their paper, one is of particular interest for us: in their words, "when M_3 was the least massive body in the system, the system invariably became unstable through the tendency of M_3 to escape from the system altogether." Accepting the McClure (1984) paradigm, we suppose that CS 22964−161 began its existence as a case 3 hierarchical triple system in which a relatively low-mass AGB progenitor (§ 8.1) was orbited by a close binary with component masses only slightly smaller than their present values, $M_1 \sin^3 i = 0.77\ M_\odot$ and $M_2 \sin^3 i = 0.68\ M_\odot$. Evidently, the distance between M_3 and the close binary was large enough to ensure stability during the lifetime of M_3. Curiously, although Kiseleva et al. (1994) made numerical simulations apparently similar to those of DM92, they make no mention of the ejection of low-mass outer components that attracted our attention to DM92.

We confine our attention to initial values of AGB mass $<2.0\ M_\odot$, adopted in accordance with the nucleosynthetic calculations in § 8.1. In the late stages of AGB evolution the system evolved from case 3 to case 1 via mass loss due to the AGB superwind. For all acceptable models in § 8.1 the mass of the WD relic for an AGB initial mass model of 1.3 $M_\odot$ is less than 0.60 $M_\odot$ (Weidemann 2000). Therefore, according to DM92, M_3 will be ejected following this ancient AGB evolution. Our extant radial velocity data suggest that the ejection already occurred. From the effect of the AGB relic on the γ velocity of CS 22964−161 calculated above we believe that this conclusion can be tested by future observations.

10. CONCLUSIONS

We have obtained high-resolution, high-S/N spectra over a 3 yr period for CS 22964−161, which was known to be metal-poor and C-rich from previous low-resolution spectroscopic studies. We discovered CS 22964−161 to be a double-line spectroscopic binary and have derived the binary orbital parameters ($P = 252$ days, $e = 0.66$, $M_p \sin^3 i = 0.77\ M_\odot$, $M_s \sin^3 i = 0.68\ M_\odot$). Both binary members lie near the metal-poor main-sequence turnoff ($T_{\mathrm{eff},p} =$ 6050 K, $\log g_p = 3.7$, and $T_{\mathrm{eff},s} = 5850$ K, $\log g_s = 4.1$). We derived similar overall metallicities for primary and secondary, $[\mathrm{Fe/H}] = -2.4$, and similar abundance ratios [X/Fe]. In particular, both stars are similarly enriched in C and the *n*-capture elements, with a clear *s*-process nucleosynthesis signature. The primary has a large Li content; the secondary's Li I feature is undetectably weak and does not usefully constrain its Li abundance.

The observed Li, C, and *s*-process abundances of the CS 22964−161 system must have been produced by an AGB star whose relic, depending on its mass, may have been ejected from the post-AGB hierarchical triple. It seems that AGB enrichment was produced by minor mass accretion in the AGB superwind rather than Roche lobe overflow. As discussed in § 8, and contrary to the thermohaline diffusion suggestion of Stancliffe et al. (2007), such hydrogen-poor accreted matter probably remained in the outer stellar layers, owing to the stabilizing μ-gradient induced by helium gravitational settling. Strong thermohaline diffusion is difficult to reconcile with the observed Li: about 9/10 of the stellar mass would be efficiently mixed on a timescale of 1 Gyr, which would imply the complete destruction of ^{7}Li because of the very high temperature

reached in the inner zones. It seems more likely that the moderate thermohaline mixing discussed in § 8, related to the effect of gravitational settling in the first 3–4 Gyr before mass accretion by the AGB donor, would save the Li from destruction. In the model of a low-mass AGB of low metallicity calculated by Domínguez et al. (2004a, 2004b) with the inclusion of "cool bottom processing" during the AGB phase, $\epsilon(\mathrm{Li}) > 3$ is achieved in the envelope. A dilution factor of about 1 dex would bring the Li abundance into accord with the observed value.

It is a pleasure to thank Guillermo Torres for sharing his TODCOR and orbit solution source code with us, Oscar Straniero for helpful discussions and continuous advice on AGB models of low mass and very low metallicity, and Noam Soker for helpful discussions on wind accretion in binary stars. We are grateful to Olivier Richard for kindly providing one of his Population II stars models, including consistently computed atomic diffusion. We thank Alan Boss, Janusz Kaluzny, Wojtek Krzeminski, and Kamil Zloczewski for obtaining photometric observations. Some of this work was accomplished while C. S. was a Visiting Scientist at the Carnegie Observatories. The hospitality and support of the observatory director are greatly appreciated. This work has been supported by the US National Science Foundation through grants AST 03-07495 and AST 06-07708 to C. S. and AST 05-07325 to I. B. T., and by the Italian MIUR-PRIN06 Project "Late Phases of Stellar Evolution: Nucleosynthesis in Supernovae, AGB Stars, Planetary Nebulae" to R. G.

REFERENCES

Allende Prieto, C., Lambert, D. L., & Asplund, M. 2002, ApJ, 573, L137
Aoki, W., Beers, T. C., Christlieb, N., Norris, J. E., Ryan, S. E., & Tsangarides, S. 2007, ApJ, 655, 492
Aoki, W., Ryan, S. G., Norris, J. E., Beers, T. C., Ando, H., & Tsangarides, S. 2002, ApJ, 580, 1149
Bate, M. R., & Bonnell, I. A. 1997, MNRAS, 285, 33
Beers, T. C., Preston, G. W., & Shectman, S. A. 1992, AJ, 103, 1987 (BPS92)
Bernstein, R., Shectman, S. A., Gunnels, S. M., Mochnacki, S., & Athey, A. E. 2003, Proc. SPIE, 4841, 1694
Bisterzo, S., Gallino, R., Straniero, O., Ivans, I. I., Käppeler, F., & Aoki, W. 2006, Mem. Soc. Astron. Italiana, 77, 985
Bondi, H., & Hoyle, F. 1944, MNRAS, 104, 273
Bonifacio, P., et al. 2007, A&A, 462, 851
Busso, M., Gallino, R., & Wasserburg, G. J. 1999, ARA&A, 37, 239
Cameron, A. G. W., & Fowler, W. A. 1971, ApJ, 164, 111
Castelli, F., Gratton, R. G., & Kurucz, R. L. 1997, A&A, 318, 841
Clayton, D. D., & Rassbach, M. E. 1967, ApJ, 148, 69
Cohen, J. G., et al. 2004, ApJ, 612, 1107
———. 2005, ApJ, 633, L109
———. 2006, AJ, 132, 137
Davies, R. E., & Pringle, J. E. 1980, MNRAS, 191, 599
Domínguez, I., Abia, C., & Straniero, O. 2004a, Mem. Soc. Astron. Italiana, 75, 601
Domínguez, I., Abia, C., Straniero, O., Cristallo, S., & Pavlenko, Y. V. 2004b, A&A, 422, 1045
Donnison, J. R., & Mikulskis, D. F. 1992, MNRAS, 254, 21 (DM92)
Gallino, R., Arlandini, C., Busso, M., Lugaro, M., Travaglio, C., Straniero, O., Chieffi, A., & Limongi, M. 1998, ApJ, 497, 388
Gallino, R., Bisterzo, S., Husti, L., Käppeler, F., Cristallo, S., & Straniero, O. 2006a, in International Symposium on Nuclear Astrophysics (Geneva: CERN), 100
Gallino, R., Bisterzo, S., Straniero, O., Ivans, I. I., & Käppeler, F. 2006b, Mem. Soc. Astron. Italiana, 77, 786
Gargett, A., & Ruddick, B. 2003, Prog. Oceanography, 56, 381
Gough, D. O., & Toomre, J. 1982, J. Fluid Mech., 125, 75
Harrington, R. S. 1975, AJ, 80, 1081
Heintz, W. 1978, Double Stars (Dordreecht: Reidel)
Helfer, H. L., Wallerstein, G., & Greenstein, J. L. 1959, ApJ, 129, 700
Hilditch, R. W. 2001, An Introduction to Close Binary Stars (Cambridge: Cambridge Univ. Press)
Huang, S. S. 1956, AJ, 61, 49
Ivans, I. I., Sneden, C., Gallino, R., Cowan, J. J., & Preston, G. W. 2005, ApJ, 627, L145
Iwamoto, N., Kajino, T., Mathews, G. J., Fujimoto, M. Y., & Aoki, W. 2004, ApJ, 602, 377
Karakas, A. I., & Lattanzio, J. C. 2003, Publ. Astron. Soc. Australia, 20, 279
Kato, S. 1966, PASJ, 18, 374
Kelson, D. D. 2003, PASP, 115, 688
———. 2008, AJ, submitted
Kiseleva, L. G., Eggleton, P. P., & Anolsova, J. P. 1994, MNRAS, 267, 161
Kurucz, R. L. 1998, in IAU Symp. 189, Fundamental Stellar Properties, ed. T. R. Bedding, A. J. Booth, & J. Davis (Dordrecht: Kluwer), 217
Landolt, A. 1992, AJ, 104, 340
Livio, M., Soker, N., de Kool, M., & Savonije, G. J. 1986, MNRAS, 218, 593
Lucatello, S., Beers, T. C., Christlieb, N., Barklem, P. S., Rossi, S., Marsteller, B., Sivarani, T., & Lee, Y. S. 2006, ApJ, 652, L37
Marigo, P., & Girardi, L. 2007, A&A, 469, 239
McClure, R. D. 1984, ApJ, 280, L31
———. 1997, PASP, 109, 536
McClure, R. D., Fletcher, J. M., & Nemec, J. M. 1980, ApJ, 238, L35
McClure, R. D., & Woodsworth, A. W. 1990, ApJ, 352, 709
McCrea, W. H. 1953, MNRAS, 113, 162
McWilliam, A. 1988, Ph.D. thesis, Univ. Texas at Austin
Mowlavi, N. 1999, A&A, 350, 73
Nollett, K. M., Busso, M., & Wasserburg, G. J. 2003, ApJ, 582, 1036
Norris, J. E., Beers, T. C., & Ryan, S. G. 2000, ApJ, 540, 456
Norris, J. E., Ryan, S. G., & Beers, T. C. 1997, ApJ, 488, 350
Peterson, R. C., Dorman, B., & Rood, R. T. 2001, ApJ, 559, 372
Preston, G. W. 1994, AJ, 108, 2267
Preston, G W., Shectman, S. A., & Beers, T. C. 1991, ApJS, 76, 1001
Preston, G. W., & Sneden, C. 2000, AJ, 120, 1014
Preston, G. W., Sneden, C., Thompson, I. B., Shectman, S. A., & Burley, G. S. 2006a, AJ, 132, 85
Preston, G. W., Thompson, I. B., Sneden, C., Stachowski, G., & Shectman, S. A. 2006b, AJ, 132, 1714
Reyniers, M., Van Winckel, H., Biémont, E., & Quinet, P. 2002, A&A, 395, L35
Richard, O., Michaud, G., & Richer, J. 2002, ApJ, 580, 1100
Rossi, S., Beers, T. C., Sneden, C., Sevastyanenko, T., Rhee, J., & Marsteller, B. 2005, AJ, 130, 2804
Sackmann, I.-J., & Boothroyd, A. I. 1992, ApJ, 392, L71
Scalo, J. M., Despain, K. H., & Ulrich, R. K. 1974, ApJ, 187, 555
Schlegel, D. J., Finkbeiner, D. P., & Davis, M. 1998, ApJ, 500, 525
Sivarani, T., et al. 2006, A&A, 459, 125
Sneden, C. 1973, ApJ, 184, 839
Sneden, C., Preston, G. W., & Cowan, J. J. 2003a, ApJ, 592, 504
Sneden, C., et al. 2003b, ApJ, 591, 936
Soker, N. 2004, MNRAS, 350, 1366
Spite, F., & Spite, M. 1982, A&A, 115, 357
Stancliffe, R. J., Glebbeek, E., Izzard, R. G., & Pols, O. R. 2007, A&A, 464, L57
Straniero, O., Domínguez, I., Cristallo, S., & Gallino, R. 2003, Publ. Astron. Soc. Australia, 20, 389
Straniero, O., Gallino, R., & Cristallo, S. 2006, Nucl. Phys. A, 777, 311
Szebehely, V., & Zare, K. 1977, A&A, 58, 145
Theuns, T., Boffin, H. M. J., & Jorissen, A. 1996, MNRAS, 280, 1264
Thorburn, J. A., & Beers, T. C. 1992, BAAS, 24, 1278
Tokovinin, A. 1997, A&AS, 124, 75
Travaglio, C., Gallino, R., Busso, M., & Gratton, R. 2001, ApJ, 549, 346
Turner, J. S. 1973, Buoyancy Effects in Fluids (Cambridge: Cambridge Univ. Press)
Turner, J. S., & Veronis, G. 2000, J. Fluid Mech., 405, 269
VandenBerg, D. A., Bergbusch, P. A., & Dowler, P. D. 2006, ApJS, 162, 375
Vauclair, S. 1999, in ASP Conf. Ser. 171, LiBeB Cosmic Rays, and Related X- and Gamma-Rays, ed. R. Ramaty (San Francisco: ASP), 48
———. 2004, ApJ, 605, 874
Veronis, G. J. 1965, Marine Res., 21, 1
Weidemann, V. 2000, A&A, 363, 647
Zucker, S., & Mazeh, T. 1994, ApJ, 420, 806